

RESEARCH ARTICLE

Abundant positively-charged proteins underlie JCVI-Syn3A's expanded nucleoid and ribosome distribution

Gesse Roure¹, Vishal S. Sivasankar¹, Roseanna N. Zia^{1*}

Department of Mechanical and Aerospace Engineering, University of Missouri, Columbia, Missouri, United States of America

☞ These authors contributed equally to this work.

* rzia@missouri.edu



OPEN ACCESS

Citation: Roure G, Sivasankar VS, Zia RN (2026) Abundant positively-charged proteins underlie JCVI-Syn3A's expanded nucleoid and ribosome distribution. PLoS Comput Biol 22(1): e1013898. <https://doi.org/10.1371/journal.pcbi.1013898>

Editor: Changbong Hyeon, Korea Institute for Advanced Study, KOREA, REPUBLIC OF

Received: August 16, 2025

Accepted: January 8, 2026

Published: January 27, 2026

Copyright: © 2026 Roure et al. This is an open access article distributed under the terms of the [Creative Commons Attribution License](https://creativecommons.org/licenses/by/4.0/), which permits unrestricted use, distribution, and reproduction in any medium, provided the original author and source are credited.

Data availability statement: The experimental ribosome position data used to validate our method were obtained from a previously published work: Goodsell, D.S., Autin, L., "Integrative modeling of JCVI-Syn3A nucleoids with a modular

Abstract

Nucleoid compaction in bacteria is commonly attributed to cytoplasmic crowding, DNA supercoiling, and nucleoid-associated proteins (NAPs). In most bacterial species, including *E. coli*, these effects condense the chromosome into a subcellular region and largely exclude ribosomes to the surrounding cytoplasm. In contrast, many *Mycoplasma*—including the *Mycoplasma*-derived synthetic cell JCVI-Syn3A—exhibit a cell-spanning nucleoid with ribosomes distributed throughout. Because *Mycoplasma* are evolutionarily distant from model bacteria like *E. coli* and have undergone extensive genome reduction, Syn3A is a natural testbed for genotype-to-'physiotype'-to-phenotype, in which genome-encoded composition reshapes cell-scale organization. Here we show that this organization can arise from Syn3A's unusually high abundance of positively charged proteins. We develop a coarse-grained model that explicitly and physically represents a sequence-accurate chromosome together with ribosomes and cytoplasmic proteins at physiological size, charge, and abundance. With DNA and ribosomes alone, the cell-spanning nucleoid relaxes toward a compacted state that sterically excludes ribosomes, indicating missing physics beyond polymer mechanics and excluded volume. When we include electrostatic interactions by assigning effective charges to each biomolecule, positively charged proteins dynamically enrich around ribosomes and DNA, partially screening ribosome–DNA repulsion. This charge shielding enables ribosomes to penetrate the nucleoid mesh and stabilizes a cell-spanning nucleoid consistent with experiment. This behavior is robust across parameter sweeps: DNA stiffness, heterogeneous mesh size, and crowding favor compaction, whereas electrostatics and size polydispersity promote expansion, with consequences for migration pathways within the nucleoid and thus transcription–translation dynamics. The framework is parameterized directly from genomic and proteomic composition and is transferable to other bacteria.

approach” Current Research in Structural Biology, 7, 100121 (2024). The dataset is available from the original publication at <https://doi.org/10.1016/j.crstbi.2023.100121>. Post-processed data and code for analysis are available on Github https://github.com/gesseroure/Syn3A_nucleoid. Dynamic simulations can be reproduced by the reader by utilizing the open-source platform LAMMPS [107].

Funding: This work was funded by the Sloan Foundation Grant Number G-2022-19561 (G.R., V.S.S., R.N.Z.). The funders had no role in study design, collection and analysis, decision to publish, or preparation of the manuscript.

Competing interests: The authors have declared that no competing interests exist.

Author summary

The chemical elements of DNA—its genes—carry the instructions for cells to grow and divide, but DNA is also a physical object packed into a crowded milieu, with organization that shapes how genetic information is accessed and used. In many bacteria such as *Escherichia coli*, the nucleoid is compacted, expelling ribosomes to the cell periphery, tending to separate transcription from translation. Yet in many *Mycoplasma*—including minimal cell JCVI-Syn3A—the nucleoid spans the entire cell, with ribosomes distributed throughout. How and why some genome-reduced bacteria adopt this expanded-nucleoid “physiotype” has remained unclear. To explore this, we built a whole-cell coarse-grained model that explicitly represents Syn3A DNA, ribosomes, and cytoplasmic proteins. The model confirms that DNA stiffness, DNA-binding proteins, and crowding all favor compaction. In contrast, we find that Syn3A’s unusually high abundance of positively charged proteins is a crucial ingredient for chromosome expansion. These proteins enrich around ribosomes and DNA, partially charge-shielding ribosomes, which enables them to enter the nucleoid mesh and stabilize a cell-spanning nucleoid. These results support a genotype-to-physiotype-to-phenotype link in which genome-encoded proteome composition reshapes the physical interactions that organize the cell interior.

Introduction

The chromosomal DNA in most bacteria is a long, closed-loop molecule that packs densely within the cell but, unlike eukaryotes, is not enclosed by a nuclear membrane. Instead, it forms a mesh-like structure that defines its own well-demarcated region. This region, called the nucleoid, contains most of the chromosome and hosts many components of gene expression within the solvent-filled “pores” of the DNA mesh. Bacterial chromosome organization spans multiple length scales, from localized bends over a few base pairs, to supercoils, to macrodomains. Structure at each of these scales shapes interactions with transcription factors and other macromolecules and thereby helps regulate gene expression. At the largest scale, the nucleoid has an overall (“global”) size and envelope. In most bacteria, including *Escherichia coli* this envelope occupies only part of the cell, leaving a surrounding DNA-poor cytoplasmic region. In such cells, ribosomes are largely excluded from the nucleoid (aside from subunits) [1–4]. This exclusion tends to separate transcription within the nucleoid from translation in the surrounding cytoplasm [5], while still permitting contexts in which ribosomes localize within or near the nucleoid periphery [6], including co-transcriptional translation.

Nucleoid compactness has direct consequences for cellular process rates. Macromolecular segregation and spatial organization can generate heterogeneous transport and encounter rates, thereby modulating reaction rates [5,7,8]; one outcome is sequestration that can accelerate mRNA translation [9–11]. Nucleoid volume and packing density also vary with growth conditions [2], and gene expression can be regulated through changes in DNA structure across scales—from local bends to

supercoils to global compaction—which can hinder or enhance access to specific genes. We refer to these links between physical organization and downstream biological outcomes as “physiotype-to-phenotype” connections. Prior experiments and models indicate that nucleoid compaction and expansion are driven in part by cytoplasmic crowding [12–21] and by nucleoid-associated proteins (NAPs) [22], a class of DNA-binding proteins functionally analogous to eukaryotic histones. NAPs remodel DNA mechanically by introducing bends [23], altering stiffness [23], and/or bridging distant segments [24,25]. Some of these local effects—such as bridging by H-NS—are known to influence global nucleoid compaction, as shown experimentally [26] and in simulations [27]. Despite this progress, key questions remain unresolved, including why some bacterial nucleoids span the entire cell.

In contrast to most bacteria, the nucleoid in some (though not all [28]) *Mycoplasma* spans the entire cell [29–31], with ribosomes distributed throughout—including within the nucleoid [32–35]. For the *Mycoplasma*-derived synthetic cell JCVI-Syn3A in particular, cryo-EM reconstructions report an approximately uniform ribosome distribution [34], but direct measurements of the nucleoid configuration remain limited, so nucleoid structure is often inferred from ribosome organization in modeling studies. *Mycoplasma* also encode far fewer nucleoid-associated proteins (NAPs) [33,36]; given the established role of NAPs in compacting and structuring bacterial chromosomes, this paucity has been proposed as a mechanistic explanation for the expanded-nucleoid organization. However, nucleoid structure is shaped not only by NAPs but also by the surrounding cytoplasm: crowding, depletion interactions, and electrostatics are all known to influence DNA compaction [37]. Disentangling how these factors combine to restructure DNA *in vivo* is important because nucleoid architecture can modulate the spatial coupling of transcription and translation during growth and environmental adaptation.

Computational modeling is a valuable complement to experiment, in part because it is challenging to dynamically image nucleoid restructuring *in vivo*. In this work, we develop a new computational model of a representative *Mycoplasma* cell to probe the physico-chemical interplay between DNA and cytoplasm that can produce an expanded nucleoid. Existing models of nucleoid formation and remodeling span a range of resolutions, from thermodynamic theories, to polymer bead–spring models embedded in mean-field backgrounds, to simulations in which DNA interacts with an explicitly represented cytoplasm. The primary distinction among these approaches is how directly they resolve DNA–DNA and DNA–cytoplasm interactions. We briefly review these frameworks, each of which has contributed to current understanding of nucleoid structure.

Thermodynamics-based approaches typically rationalize DNA restructuring through two related lenses: polymer collapse and phase separation. De Gennes’ foundational work on polymer collapse emphasized the role of solvent quality in driving condensation [38], motivating many subsequent theories. Post and Zimm developed an early thermodynamic description of nucleoid formation by treating distinct coiling motifs as phases [39]. De Vries extended solvent-quality ideas to include the effects of cytoplasmic crowders [40]. Odijk later proposed a liquid-like phase-separation picture in which supercoils condense via depletion interactions induced by crowders [41], consistent with experimental observations of crowder-induced compaction [12]. Because these theories are computationally inexpensive, they remain widely used and often serve as benchmarks for higher-resolution simulations [42–44]. Their key limitation is that they effectively average over local spatial structure, obscuring *local* crowding, heterogeneous accessibility, and explicit DNA interactions that can modulate gene activity.

Dynamical models of DNA span a wide range of physical resolutions, from atomistic simulations that resolve local structure to continuum theories that capture system-level, far-from-equilibrium behavior. At the smallest scales, near-atomistic and all-atom simulations resolve conformational fluctuations of DNA and associated biomolecules [45–48]. These approaches can directly interrogate mechanisms such as NAP–DNA binding that induces local bending and bridging, as well as the condensing action of ions, amino acids, and polypeptides [49–52]. Coupled with recent AI advances such as AlphaFold [53], atomistic modeling has transformed structural biology, enabling high-fidelity views of protein conformational dynamics [54–56] and of how binding events remodel local DNA structure [57]. However, atomistic simulations remain prohibitively expensive for cell-scale chromosome organization: even with coarse-graining steps, studies of DNA–protein binding typically focus on segments shorter than ~100 bp [58], and predicting cooperative deformation

of the full bacterial nucleoid is beyond the reach of all-atom models alone. Multiscale strategies that combine atomistic detail with coarse-grained representations are therefore essential for extending these insights to longer DNA and more complex assemblies [59–61].

At the opposite extreme, continuum theories describe global nucleoid behavior away from equilibrium by averaging over microscopic detail. Examples include field-theoretical descriptions of diffusion [62] and active-fluid models of chromatin transport [63]. These approaches have yielded important insights into emergent phenomena, including swelling driven by competition between coiling and diffusion in bacterial chromosomes [62] and flow-driven coalescence of chromatin in eukaryotic nuclei [63,64]. Because they do not resolve local structure, however, continuum models are not designed to connect specific molecular binding events to heterogeneous changes in nucleoid microstructure. Bridging these local and global descriptions motivates intermediate-resolution, mesoscale modeling.

Mesoscale biophysical models are well suited to provide this bridge. Coarse-grained polymer frameworks represent DNA and other macromolecules as bead–spring chains of colloid-like particles, retaining explicit excluded-volume and other local interactions while remaining tractable at chromosome length scales [65]. When embedded in an explicitly represented cytoplasm, mesoscale models can link multi-scale DNA remodeling to cell-wide biomolecular organization and transport.

Bead–spring polymer models have been used to capture a broad range of chromosome-level phenomena, including supercoiling dynamics [66–68], knotting [69], replication [70], condensation [71], and macromolecular transport within phase-separated domains [72]. This combination of local physical resolution with cell-scale reach has made mesoscale models a powerful tool for studying nucleoid compaction and cytoplasmic organization. For example, Sottas et al. [67] showed that dynamical supercoiling and salt concentration influence plasmid compaction, and Joyeux demonstrated that confinement and crowding can compact a generic bead–spring nucleoid even in the absence of supercoiling [73]. Subsequent model improvements incorporated supercoiling and DNA-bridging proteins, which were shown to induce further compaction [27,74]. Related simulations introduced additional effects such as crowder-size bidispersity and non-spherical confinement [3,4,20]. In contrast to thermodynamic theories, these approaches retain explicit local interactions with crowdors and bridging proteins. A recent combined experimental and mesoscale simulation study in *E. coli* further demonstrated how nucleoid structure and charge influence macromolecular diffusion and segregation [8]. Overall, physically resolved coarse-grained models have clarified how nucleoid structure responds to cytoplasmic interactions and, conversely, how nucleoid features shape biomolecular organization.

Despite this progress, it remains unclear why the nucleoid is persistently compact in many bacteria, yet expands to fill the entire cell in others. These distinct global states correlate with markedly different cell-wide biomolecular organization, but the direction of causality is unresolved: does nucleoid architecture impose a particular spatial organization of the cytoplasm, or do cytoplasmic composition and interactions set nucleoid architecture? Two additional ingredients are especially likely to influence both compaction and segregation: electrostatic charge and size polydispersity, which together can promote clustering, condensate formation, and selective partitioning [75,76].

Recent physically resolved whole-cell models of *Mycoplasma*-derived synthetic cells achieved remarkable chromosomal detail, including 10 bp-resolution reconstructions of complete genomes and replication dynamics [70], and extensions incorporating RNA polymerase (RNAP) to visualize cell organization [77]. However, both studies model only DNA, ribosomes, and a simplified cytosol: they omit the cytoplasmic proteome, neglect electrostatic interactions, and do not include HU proteins. In addition, ribosomes are placed directly from experimental distributions; the chromosome is then assembled into the remaining space (and, in [77], RNAPs are added prior to DNA assembly). Under this construction protocol, a cell-spanning nucleoid follows unavoidably because the interior volume is effectively reserved for DNA during assembly. By contrast, in a physiological cytoplasm, the missing components—a dense, size-polydisperse proteome with heterogeneous charge—can be expected to strongly reshape both nucleoid microstructure and global extent. Indeed, Syn3A is striking in this regard: its proteome is strongly charge-skewed, with a substantially larger fraction of positively charged proteins than in *E. coli* (nearly the inverse composition), suggesting that electrostatics may be a key, genome-encoded

determinant of the expanded-nucleoid physiotype. These considerations motivate incorporating both cytoplasmic proteins and electrostatic interactions into whole-cell models to directly test how composition and physical interactions jointly set nucleoid organization.

In this study, we use a mesoscale whole-cell model to test which physical mechanisms can sustain an expanded-nucleoid physiotype in a *Mycoplasma*-type cell. We focus on the *Mycoplasma*-derived synthetic minimal cell JCVI-Syn3A, engineered to retain only the genome required for life [78,79]. Recent cryo-EM reconstructions report an approximately uniform ribosome distribution in Syn3A [34], consistent with the cell-spanning nucleoid organization observed across several *Mycoplasma* [32,33,35], and motivating prior models that assume an expanded nucleoid [34,70,77]. Here we move beyond DNA–ribosome-only, charge-neutral descriptions by explicitly representing cytoplasmic proteins and incorporating HU-mediated DNA bending and electrostatic interactions, enabling a direct, mechanistic test of how genome-encoded composition reshapes nucleoid organization. Because the model is parameterized from genomic and proteomic composition, the framework is readily transferable to other bacteria as such data become available [80].

Results and discussion

Recapitulating experiment-matched models

As a starting point, we asked whether the experiment-matched spatial organization reported for Syn3A can be sustained by the simplest physically resolved model containing only DNA and ribosomes. We therefore began from the ribosome distribution reported by [34], which also underlies prior Syn3A reconstructions [70,77]. In those studies, ribosomes were placed according to experiment, held fixed, and the chromosome was assembled into the remaining volume. Using the same protocol with our swelling Monte Carlo algorithm, we generated an experiment-informed initial condition with an approximately uniform ribosome distribution and a cell-spanning nucleoid (Fig 1A). As in [70], this minimal system includes only DNA, ribosomes, and entropic exclusion (see *Methods*).

Gilbert et al. [34,70] do not explicitly distinguish individual ribosomes from polysomes; their cryo-EM analysis reports the total ribosome population, irrespective of whether a ribosome is translating as a single particle or as part of a polysome. Image processing in JCVI-Syn3A indicates that approximately 25–55% of ribosomes are polysomal at a given time [34]. Thus, Fig 1 should be interpreted as a coarse-grained, population-level view of the combined single-ribosome and polysomal signal relative to the nucleoid. In the present work, we model ribosomes as independent coarse-grained macromolecules representing this total population. This approximation allows us to focus on mesoscale organization of DNA, ribosomes, and protein electrostatics, while explicit polysome architecture is deferred to future work. The potential contribution of polysomes is discussed in the Concluding Remarks.

This construction protocol reproduces the experimentally reported ribosome distribution by design, but it does not establish that the configuration is dynamically stable. Indeed, entropic exclusion alone is known to drive ribosome segregation and nucleoid compaction [73]. To test stability, we initiated Brownian dynamics from the experiment-informed configuration. The system rapidly relaxes to the state in Fig 1B: ribosomes migrate substantially (though not completely) toward the cell periphery, and the nucleoid moderately compacts, evidenced by a DNA-poor region near the membrane and an increased DNA density toward the cell center.

To check whether this outcome depends on the experiment-based initialization, we also generated DNA and ribosome configurations *ab initio*, without imposing the measured ribosome positions. Using our swelling Monte Carlo procedure to assemble the chromosome while initializing all particles uniformly, we obtain the configuration in Fig 1C. Strikingly, it is qualitatively similar to the dynamically evolved experiment-informed case in Fig 1B: ribosomes again accumulate near the membrane and the nucleoid becomes modestly compacted. Together, Fig 1 shows that, with only hard-sphere (entropic) interactions [70], ribosomes are naturally driven out of the nucleoid and the nucleoid compacts by at least ~15% in volume. This behavior is inconsistent with the near-homogeneous ribosome distribution observed in Syn3A [34], indicating that a DNA–ribosome-only, charge-neutral model is missing key physics.

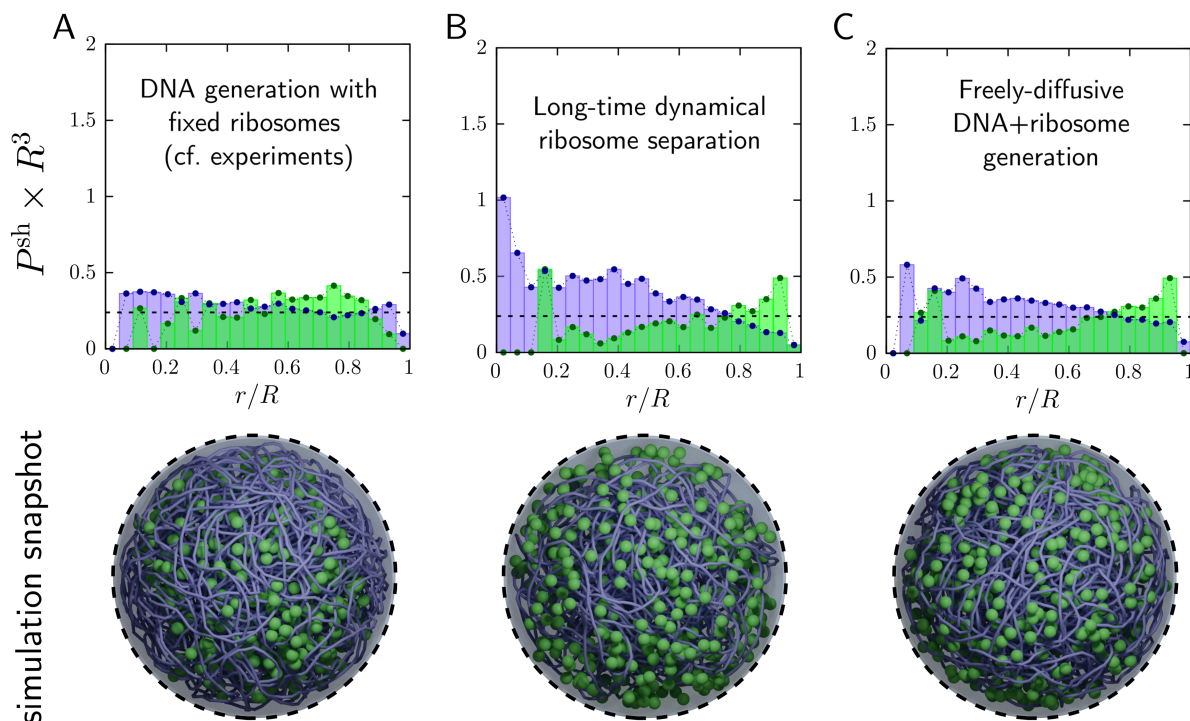


Fig 1. Nucleoid and ribosome spatial configurations predicted by our simplest computational model of JCVI-Syn3A, containing only DNA and ribosomes (both charge neutral). Following the ribosome data reported by [34], this model includes 503 ribosomes and a chromosome coarse-grained at 100 bp/bead. Top row: Probability per unit volume of finding a DNA bead (purple) or ribosome (green), binned into annular shells from the center ($r/R = 0$) to the membrane ($r/R = 1$) in simulations (total volume fraction $\phi = 0.099$). (A) Experiment-informed initial condition (no dynamics), constructed to match [34]. Both DNA and ribosomes appear approximately homogeneous throughout the cell. (B) Same initial condition as (A) after Brownian dynamics with entropic exclusion. DNA compacts toward the center and ribosomes redistribute toward the periphery, demonstrating that a DNA–ribosome-only, charge-neutral model does not sustain the experimentally inferred organization. (C) Self-assembled initial condition generated without experimental placement: DNA beads and ribosomes are initialized uniformly, after which DNA is assembled into a single closed loop via the swelling Monte Carlo algorithm (see *Methods*). The system again relaxes toward compaction and ribosome redistribution, showing that the outcome is robust to the initialization protocol and reinforcing that DNA and ribosomes alone are insufficient to recover the experimentally inferred homogeneous distribution. Bottom row: Simulation snapshots with 503 ribosomes and a sequence-accurate nucleoid, coarse-grained to 100 bp/bead (smoothed for visual clarity).

<https://doi.org/10.1371/journal.pcbi.1013898.g001>

Syn3A contains many additional biomolecules with heterogeneous sizes and charges, as well as nucleoid-associated proteins. Beyond the proteome’s physiological packing fraction and charge distribution, Syn3A is also reported to have a low abundance of nucleoid-associated proteins (personal communication, John I. Glass, J. Craig Venter Inst.), which has been proposed as a contributor to its expanded-nucleoid organization. In the remainder of the Results, we therefore incorporate additional, physiologically motivated mechanisms and assess their effects on macromolecular organization: intrinsic DNA stiffness, HU-induced DNA bending, cytoplasmic crowding, and electrostatic interactions, and how each reshapes DNA–ribosome–protein distributions in Syn3A.

Nucleoid stiffness can induce DNA compaction

Base-pair stacking, mediated by chemical bonding, underlies DNA’s intrinsic multiscale structure and gives rise to mesoscale material properties such as bending, stretching, and torsional stiffness [81,82]. As with synthetic polymers, these intrinsic material properties are expected to influence the nucleoid’s global size and compactness. More generally, the chromosome comprises both DNA and bound proteins that can further modify local curvature and effective

stiffness. In our model, these effects are captured through the dimensionless stiffness coefficients σ_s and σ_b , which set the chromosome's resistance to stretching and bending, respectively (see *Methods*, Eqs (4)–(5), and Fig 8).

For the conceptual overview and experimental validation in Fig 1, we base our depiction of nucleoid and ribosome organization on the imaging [34] and modeling study of Gilbert et al. [70], which, to our knowledge, is the only work that provides spatially resolved measurements of ribosome distributions in JCVI-Syn3A together with an explicit physical model. This dataset anchors our qualitative description of chromosome–ribosome organization. In contrast, the quantitative parameters for protein identity, abundance, and net charge used in our simulations are derived from the JCVI-Syn3A proteomics of Breuer et al. [79], which provide comprehensive proteome composition but no spatial localization. Thus, Gilbert et al. supply the spatial context for Fig 1, whereas Breuer et al. supply the detailed proteomic information needed to parameterize the protein components of our model. These two datasets are therefore complementary: one constrains spatial organization, and the other constrains composition and charge. Our baseline model for the remainder of the study is thus built using data published by Breuer *et al.*, selected for its comprehensive proteomics [79] (see Table 1 in *Methods*).

We therefore consider a baseline Syn3A model with 600 ribosomes and an intrinsic DNA bending stiffness set by base-pair stacking; explicit binding proteins are introduced in the next section. For “bare” DNA (i.e., in the absence of nucleoid-associated proteins), we set the bending stiffness coefficient to $\sigma_b = 10$, consistent with established theoretical and experimental estimates [82]. Similar values have been used in recent coarse-grained models with simplified cytoplasmic constituents [27,83] as well as Syn3A [70]. Because changing σ_b can either expand or compact the chromosome globally, we simulated a range of bending stiffness values and quantified the resulting DNA and ribosome spatial distributions. Fig 2A shows representative snapshots for a soft nucleoid ($\sigma_b = 0$), a moderately stiff nucleoid ($\sigma_b = 10$) corresponding to physiological conditions, and a stiff nucleoid ($\sigma_b = 50$). To obtain adequate statistics and minimize sensitivity to knotting and kinetic trapping, we average results over 100 simulations and compute ensemble-averaged radial distributions of DNA beads and ribosomes (see *Methods*).

Fig 2B shows that intrinsic bending stiffness influences both nucleoid compactness and ribosome localization. Increasing σ_b leads to a more compact chromosome and a stronger redistribution of ribosomes away from DNA-rich regions: the stiffer the nucleoid, the more ribosomes are depleted from the cell interior. Even in the softest case ($\sigma_b = 0$), however, a DNA-poor peripheral region persists and is preferentially occupied by ribosomes. Overall, varying inherent DNA stiffness alone does not recover the near-homogeneous ribosome distribution inferred from experiment in the simplified DNA–ribosome models used here and previously [34,70]. Moreover, reducing stiffness from $\sigma_b = 10$ to $\sigma_b = 0$ produces only modest changes in macromolecular organization, whereas a large increase to $\sigma_b = 50$ yields an extended DNA-depleted layer near the membrane populated almost exclusively by ribosomes, along with near-complete ribosome depletion from the cell center. We return to the mechanistic origin of these trends in later sections, where we interpret them in terms of competition between entropic exclusion and the energetic cost of bending a stiff polymer.

These results are obtained in a deliberately simplified setting—without electrostatics, without proteomic crowding, and without nucleoid-associated proteins such as HU, which are known to remodel DNA bending stiffness *in vivo* and *in vitro* [84]. Before adding these missing components, we first examine how intrinsic stiffness couples to DNA microstructure and to the ribosome distributions observed in Fig 2.

Nucleoid pore distribution partly explains ribosome exclusion

The stiffness-dependent ribosome redistribution in Fig 2 suggests that nucleoid *microstructure*—in particular, its pore-size (mesh-size) distribution [86]—may help determine where ribosomes can reside. To quantify this porous structure, we performed a Voronoi-based analysis following [85], with modifications to account for membrane confinement. As illustrated in Fig 3A, we compute a Voronoi tessellation in the void space excluded by DNA and the confining membrane, yielding a network of edges (green) that traces connected pore pathways. Each edge E_i is associated with a local void segment

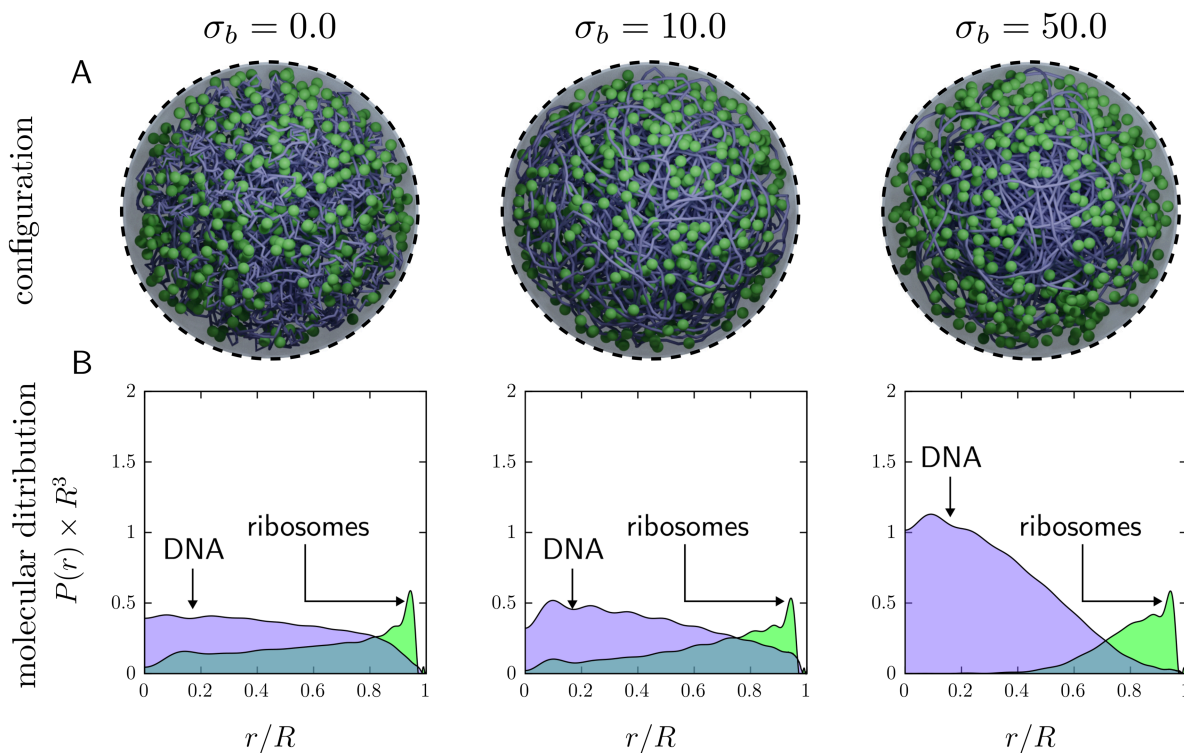


Fig 2. Impact of intrinsic nucleoid stiffness on the spatial distributions of DNA and ribosomes. The bending stiffness σ_b (values shown at top) is applied uniformly to all DNA triplets. (A) Simulation snapshots (total volume fraction $\phi = 0.079$). Ribosomes: green spheres. DNA: purple (100 bp/beat; smoothed for visual clarity). (B) Radial distributions of DNA beads (purple) and ribosomes (green), from the cell center to the membrane, averaged over 100 independent simulations.

<https://doi.org/10.1371/journal.pcbi.1013898.g002>

whose characteristic diameter d_i sets the size of the largest spherical particle that can occupy (or traverse) that segment. We exclude edges near the membrane that produce spuriously small or ill-defined voids.

Fig 3B shows that increasing bending stiffness progressively reorganizes nucleoid microstructure, with apparent increase in persistence length, i.e. the length over which a segment extends like a rod with little curvature (see Fig B in S1 Text for persistence length results). Confinement together with stiffness produces a pronounced DNA-depleted region near the membrane, with DNA enriched toward the cell interior; this trend is amplified at larger σ_b , consistent with prior observations for confined semiflexible polymers [87]. Simulations of DNA alone (no ribosomes or proteins) show the same center-enriched, wall-depleted pattern (see Fig F in S1 Text), indicating that it arises from polymer mechanics under confinement rather than from excluded-volume interactions with other macromolecules. The dashed contours in Fig 3B (enclosing 95% of DNA) and the reported radius of gyration (R_g) values further indicate that lower intrinsic stiffness expands the global nucleoid envelope.

We next quantified pore sizes across 100 realizations at each stiffness. The pore-size distributions in Fig 3C exhibit a dominant pore scale for each σ_b , with a weak tail toward larger pores. For the stiffest nucleoid, most pores are smaller than a ribosome diameter, consistent with the strong ribosome depletion observed at $\sigma_b = 50$ in Fig 2. For $\sigma_b = 0$ and $\sigma_b = 10$, the *global* distributions are similar, despite visible differences in microstructure in Fig 3B; this similarity reflects the fact that panel (C) averages pore sizes over the entire nucleoid.

The key distinction emerges when pore sizes are resolved spatially. We therefore computed the mean local pore diameter $\langle d \rangle(r)$ as a function of distance r from the cell center by sampling Voronoi edges that intersect a spherical surface

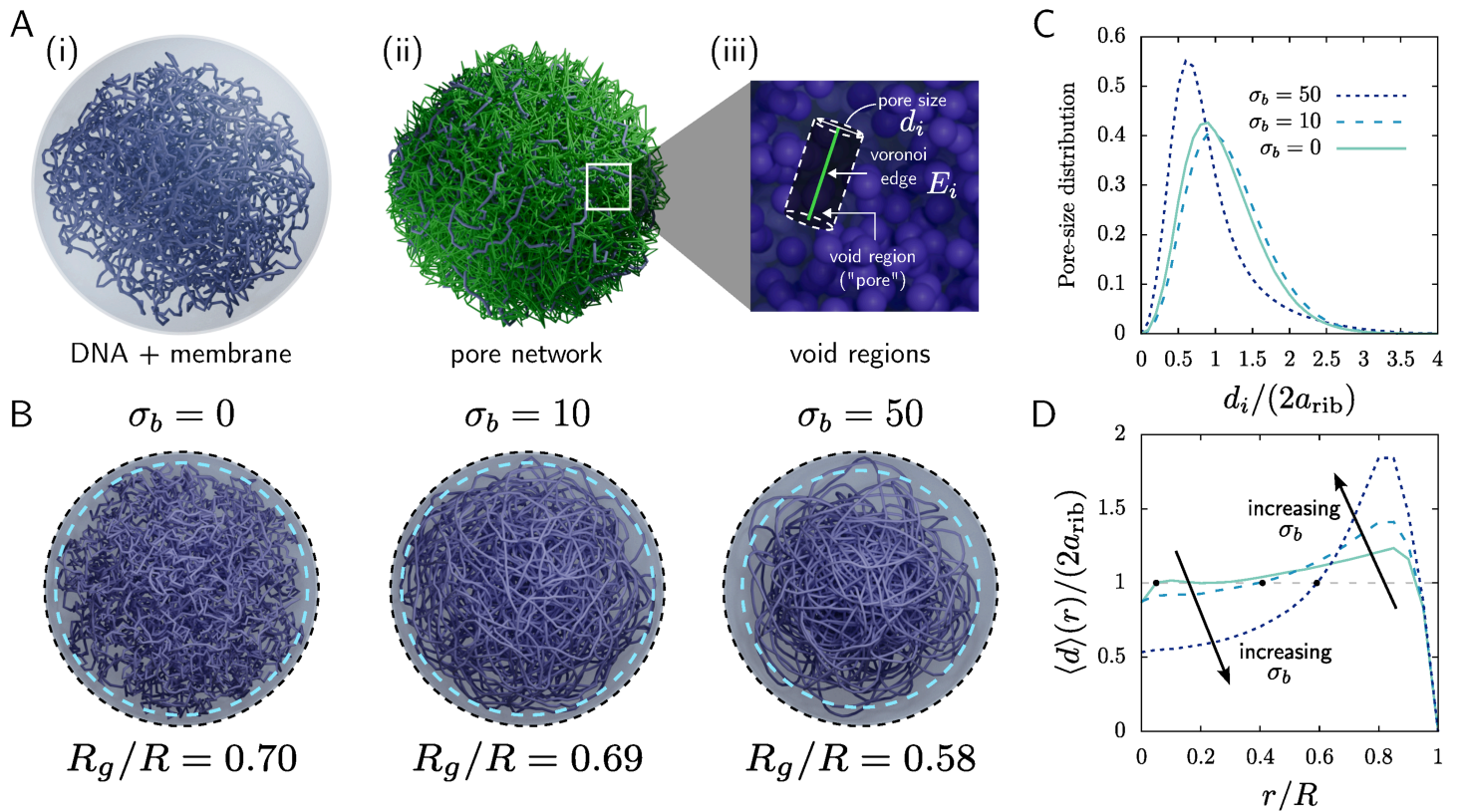


Fig 3. Voronoi analysis of nucleoid pores (mesh size) for three values of bending stiffness, as indicated in legends. (A) Voronoi interrogation of the nucleoid. (i) Simulation image showing only the DNA and enclosing membrane (ribosomes made invisible for visual clarity). (ii) Voronoi tessellation throughout the nucleoid. The resulting (infinitesimally thin) edges, shown in green, traverse the interconnected voids within the nucleoid. (iii) Determination of the radius d_i (pore size) of a void segment centered around a Voronoi edge E_i . (B) Visualization of nucleoid structure for three values of bending stiffness. The resulting radius of gyration R_g/R , normalized on total cell radius, is shown below each image. Dashed blue lines enclose 95% of DNA, with values $R_{95}/R = 0.93, 0.94, \text{ and } 0.864$ from less to more stiff. (C) Distribution of pore sizes d_i (normalized on ribosome diameter) in the nucleoid [85]. (D) Average size $\langle d \rangle(r)$ of void segments located at distance r from the center of the cell, calculated using Eq (1). For both (C) and (D) we use data from 100 realizations.

<https://doi.org/10.1371/journal.pcbi.1013898.g003>

S_r of radius r and averaging their associated diameters:

$$\langle d \rangle(r) = \frac{1}{N_r} \sum_{E_k \cap S_r \neq \emptyset} d_k, \quad (1)$$

where N_r is the number of edges intersecting S_r . Fig 3D shows that increasing stiffness enhances spatial heterogeneity: pores become smaller in the nucleoid interior and larger near its periphery. In particular, increasing σ_b from 0 to 10 reduces $\langle d \rangle(r)$ near the center while increasing it toward the nucleoid edge, even though the globally averaged distributions in Fig 3C change only weakly.

Together, these results suggest that ribosome exclusion is governed not simply by DNA concentration but by the stiffness-controlled mesh geometry of the nucleoid. For the stiffest nucleoid, the average pore size near the center is well below a ribosome diameter, consistent with ribosome depletion from the cell interior. For the softer nucleoids, central pore sizes are closer to ribosome scale, which may permit transient entry and trapping (see S1 Text).

Gene accessibility, migration pathways and compactness

Pore-size distributions quantify nucleoid microstructure, but they do not by themselves determine whether macromolecules can *move through* the nucleoid to reach specific loci. Long-range accessibility depends on the connectivity of pores into continuous, tortuous pathways: a molecule may fit locally yet still be unable to traverse the mesh if admissible pores do not percolate. Conversely, sufficiently small particles may explore most of the nucleoid, whereas larger particles may penetrate only partway before becoming confined to an isolated void network. To quantify this size-dependent accessibility, we use the Voronoi network constructed above and identify pathways that can be traversed by a spherical particle of radius a , following [85]. Specifically, we prune the Voronoi graph by retaining only edges with local diameter $d_i \geq 2a$ and then use a graph-traversal algorithm to extract connected components of the remaining network. Each connected component defines a *traversable region*—a portion of the nucleoid mesh within which a particle of size a can move without geometric obstruction (see Fig 4A). Depending on a , the pruned network may contain a single percolating component or multiple disconnected regions, implying either cell-scale accessibility or size-dependent trapping.

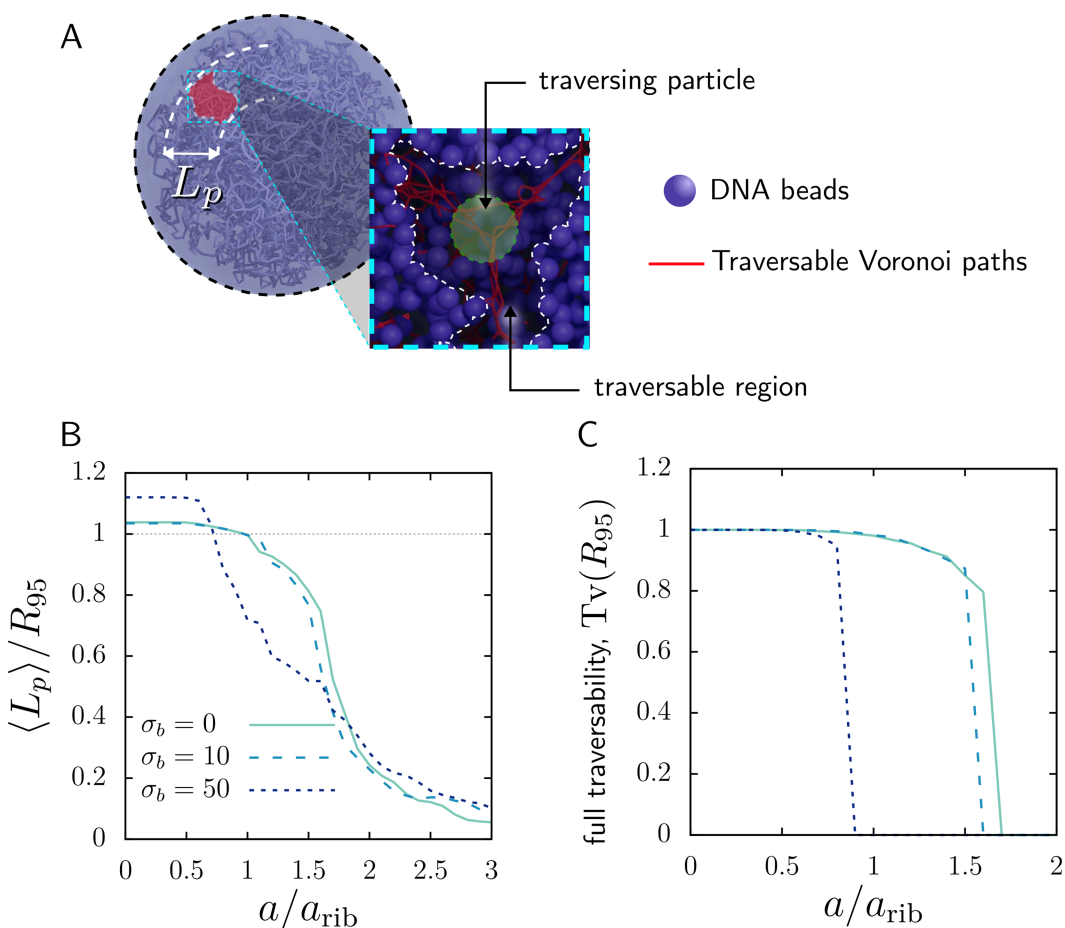


Fig 4. Traversability analysis of the nucleoid mesh for three values of bending stiffness σ_b . (A) Schematic of a biomolecule moving through a traversable region inside the nucleoid. The penetration length $\langle L_p \rangle$ (see annotation) quantifies the *radial* extent of that region, i.e., the fraction of the distance from center to edge of the nucleoid that is accessible along connected pore pathways. (B) Average penetration length $\langle L_p \rangle$ normalized by the radius enclosing 95% of DNA content, R_{95} , as a function of macromolecular size. Angle brackets denote an average over all traversable regions (see *Methods*). (C) Fraction T_v (Eqs (19) and (20)) of pathways that are fully traversable from center to edge (i.e., $L_p \geq R_{95}$), giving the likelihood that a molecule can traverse the entire nucleoid.

<https://doi.org/10.1371/journal.pcbi.1013898.g004>

The traversable regions, penetration lengths, and full-traversability fractions reported here quantify nucleoid accessibility in a statistical ensemble sense: they characterize the connectivity of the mesh across many equilibrated configurations that a fluctuating nucleoid is expected to sample over time, rather than the lifetime of any individual pore in a single trajectory. This provides a time-averaged view of which migration pathways are typically available to molecules of a given size. Explicitly coupling this structural analysis to time-resolved chromosome–transport simulations remains an important direction for future work.

We summarize each traversable region by its penetration length L_p , defined as the radial span accessible within that connected component (see Fig 4A). Intuitively, L_p measures how far a particle can move radially through connected pore space—from its most outward accessible location toward the center (and vice versa). We computed L_p for particle sizes spanning $0 \leq a \leq 3a_{\text{rib}}$. Fig 4B shows that, on average, smaller particles penetrate deeper, and that reduced stiffness ($\sigma_b = 0$ and 10) modestly increases penetration compared to $\sigma_b = 50$. For all stiffness values, particles must be smaller than $\sim 1.75 a_{\text{rib}}$ to penetrate beyond $\sim 40\%$ of R_{95} , whereas very small values of $\langle L_p/R_{95} \rangle$ indicate effective exclusion or confinement to a small, isolated void.

Connectivity can also be summarized by the fraction of pathways that are fully traversable across the nucleoid. We therefore quantify the likelihood that a particle lies in a component with $L_p \geq R_{95}$, reported as Tv in Fig 4C. As in percolation phenomena [88] and in related Voronoi analyses [85], increasing particle size produces a geometric transition at a *critical size* beyond which fully traversable pathways become rare. The mild decay of Tv below unity for intermediate sizes indicates occasional trapping in disconnected pore components, whereas beyond the steep drop past the critical size, full traversal becomes unlikely. For $\sigma_b = 0$ and 10, the critical sizes are $\sim 1.6 a_{\text{rib}}$ and $\sim 1.75 a_{\text{rib}}$, respectively, implying that ribosome-sized particles can often access connected pathways spanning most of the nucleoid in this simplified, charge-neutral model. In contrast, increasing stiffness to $\sigma_b = 50$ reduces the critical size to $\sim 0.8 a_{\text{rib}}$, consistent with strong ribosome exclusion from the nucleoid interior in Fig 2.

Overall, at the physiological stiffness modeled here for Syn3A ($\sigma_b = 10$) and in the absence of electrostatics and cytoplasmic proteins, the nucleoid mesh remains broadly connected for a wide range of particle sizes, even though the nucleoid is globally compacted and a DNA-poor peripheral region persists.

In the next sections we incorporate additional, biologically motivated mechanisms omitted thus far—including DNA-bending proteins, cytoplasmic crowding, and electrostatics—and test how they reshape both nucleoid compactness.

Local HU-induced bends induce further nucleoid compaction

The stiffness results above show that intrinsic DNA mechanics can compact the nucleoid and thereby bias ribosomes toward DNA-poor regions. Nucleoid architecture, however, is also shaped by DNA-binding proteins that locally remodel the polymer. Syn3A encodes only one nucleoid-associated protein (NAP), HU [89], which can stiffen DNA and induce sharp local bends [23]. Because *Mycoplasma* are reported to carry far fewer NAPs than many bacteria [36], HU scarcity has been proposed as an explanation for the expanded-nucleoid phenotype.

Here we test that hypothesis directly by incorporating HU-mediated bends into our model. Unlike bridging NAPs such as H-NS [27], HU primarily acts locally: depending on binding mode, it increases local stiffness and/or imposes a preferred bend angle over a short DNA segment [23] [Fig 5A]. We model HU by introducing randomly distributed local *bending defects* along the genome (see *Methods*), corresponding to a prescribed HU copy number N_{HU} .

Fig 5B–5D shows that increasing N_{HU} progressively compacts the nucleoid, reduces pore sizes, and enhances ribosome redistribution toward the periphery—a mechanistic signature consistent with HU’s local bending action. Importantly, at the physiologically relevant HU abundance for Syn3A ($N_{\text{HU}} = 50$), we observe little additional compaction relative to the bare-DNA baseline: HU at native levels does *not* further exacerbate nucleoid compaction in this simplified, charge-neutral model. Substantial compaction arises only for HU abundances well above Syn3A’s reported levels (but closer to

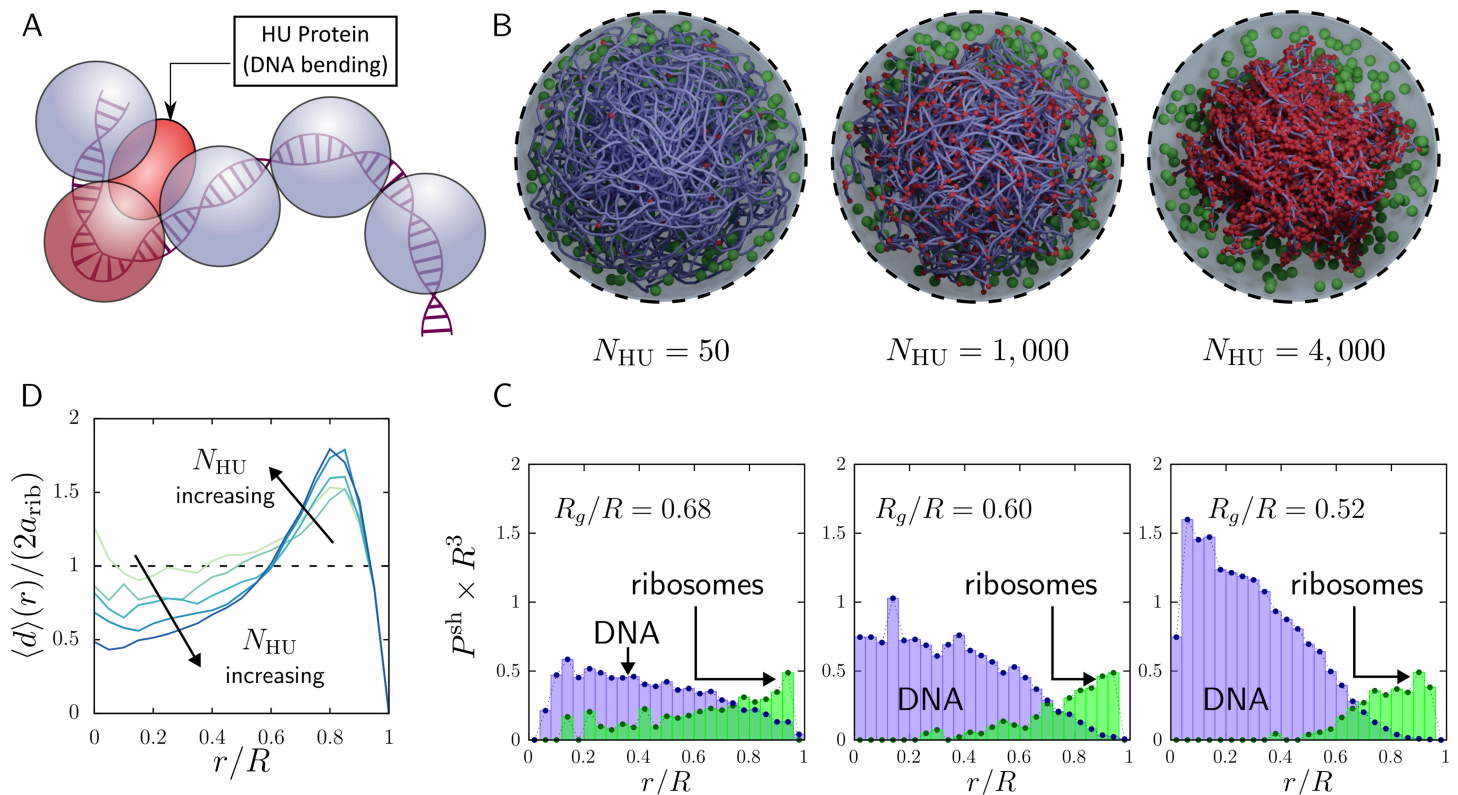


Fig 5. Influence of DNA-bending HU proteins on nucleoid compactness. (A) Schematic: HU binding induces a local bend characterized by a local stiffness σ_b^{HU} and equilibrium angle θ_{HU} that differs from the global $\theta_0 = \pi$. To mimic sequence-independent binding, bends are placed at random genomic locations (see *Methods*). Here we impose $\sigma_b = \sigma_b^{\text{HU}} = 10$ and $\theta_{\text{HU}} = 2\pi/3$ while systematically varying HU copy number N_{HU} as indicated. (B) Simulation snapshots for increasing N_{HU} . (C) Radial distributions of DNA (purple) and ribosomes (green). (D) Mean pore diameter $\langle d \rangle(r)$ versus radius, computed using Eq (1).

<https://doi.org/10.1371/journal.pcbi.1013898.g005>

those typical of other bacteria [36]). Thus, within our modeling assumptions, HU scarcity can be viewed as *permissive* for a cell-spanning nucleoid, but it is not, by itself, a sufficient mechanism to generate expansion.

More broadly, this HU “dose response” provides a quantitative handle for tuning nucleoid microstructure and accessibility *in silico*, suggesting a potential control knob for synthetic-biology design of chromosome organization. Having established that physiologically realistic HU levels do not resolve the discrepancy with experiment, we next incorporate the dominant missing component in prior Syn3A models: the remainder of the cytoplasmic proteome and its crowding effects.

Cytoplasmic proteins entropically exclude ribosomes from the nucleoid

Up to this point, our model—as in [70]—included only DNA and ribosomes. Yet cytoplasmic proteins are a major source of crowding, and crowding is known to compact bacterial DNA through entropic (excluded-volume) effects in experiments [12,15,17,21] and simulations [73]. Here we therefore add Syn3A’s cytoplasmic proteins at physiologically relevant abundance, while still treating all macromolecules as charge neutral, to isolate the effect of protein crowding. To avoid conflating crowding with proteome-wide size polydispersity, we represent cytoplasmic proteins using a single average radius derived from the Syn3A proteome (see *Methods*).

Building on the baseline composition used above, we introduce proteins using the swelling Monte Carlo initialization (see *Methods* and *S1 Text*). Fig 6A and 6B recapitulates the charge-neutral DNA–ribosome model with 600 ribosomes. We then construct a more physiological composition by adding cytoplasmic proteins at the relative abundance reported for Syn3A at growth rate 0.396 db/hr [79], which increases the total macromolecular volume fraction to $\phi = 10.4\%$ (up from $\phi = 7.9\%$ in the ribosome–DNA-only baseline). The resulting configuration (Fig 6C and 6D) shows markedly stronger nucleoid compaction and a pronounced redistribution of ribosomes toward the cell periphery, accompanied by a widened DNA-depleted annulus near the membrane. Notably, the magnitude of this crowding-induced compaction is comparable to that produced by a highly stiff chromosome in Fig 2 (e.g., $\sigma_b = 50$), underscoring that explicitly representing cytoplasmic proteins—often omitted in whole-cell simulations—substantially reshapes nucleoid organization.

A simple explanation would be that proteins compact the nucleoid merely by increasing the total volume fraction. To test whether volume fraction alone accounts for the effect, we performed a control simulation of the DNA–ribosome-only model at the same total volume fraction as the protein-containing case (Fig 6D), replacing (D)’s proteins with additional ribosomes (which are nearly five-fold larger by radius). In this control (Fig 6E), ribosomes interpenetrate the nucleoid more extensively and the nucleoid expands to accommodate them. Thus, the compaction in Fig 6C and 6D cannot be attributed solely to an increased ϕ ; rather, it depends strongly on the presence of *smaller* crowders.

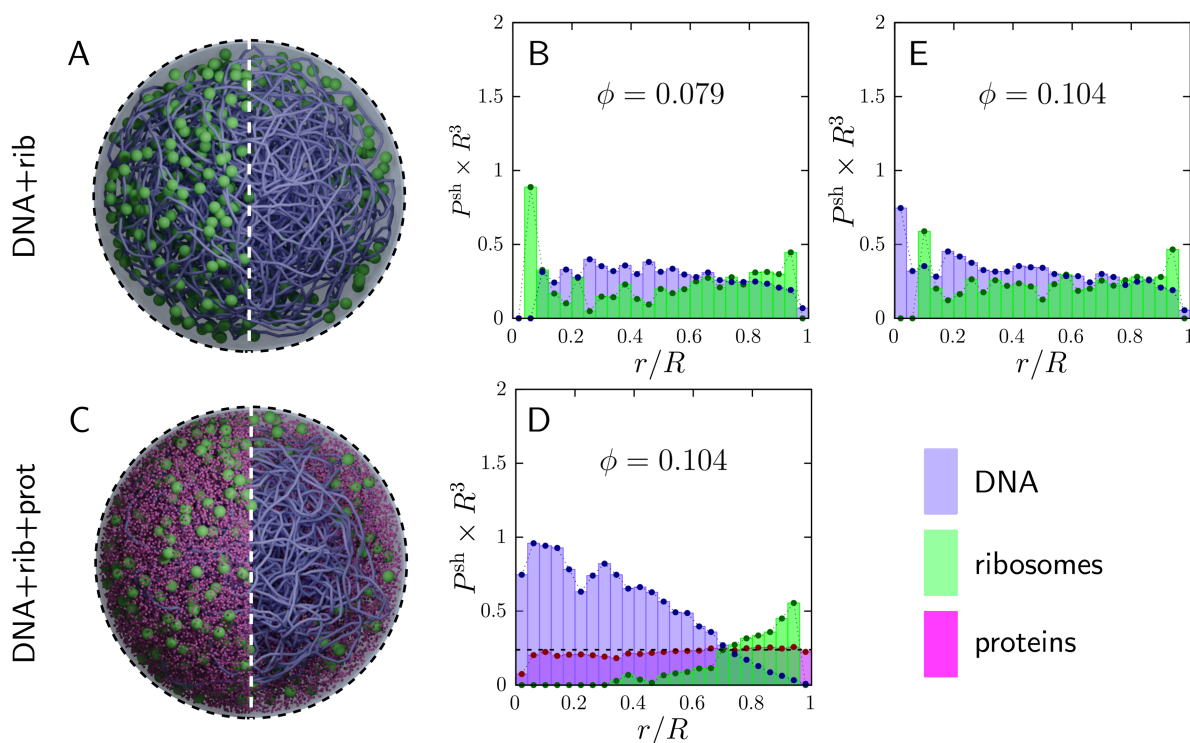


Fig 6. Dynamic simulations of the Syn3A model cell containing a coarse-grained chromosome and 600 ribosomes, with and without an explicit pool of cytoplasmic proteins (all macromolecules charge neutral). Top row (DNA+rib only): (A) & (B) show baseline model with $\phi = 0.079$ (middle panel of Fig 2). (A) representative simulation snapshot and (B) radial probability densities $P^{\text{sh}}(r)$ (scaled by R^3) for DNA (purple) and ribosomes (green) as a function of normalized radius r/R (cell radius R). Bottom row (DNA+rib+prot): model with DNA, ribosomes, and cytoplasmic proteins at $\phi = 0.104$ and growth rate 0.396 db h^{-1} , showing (C) a representative snapshot and (D) the corresponding profiles for DNA (purple), ribosomes (green), and proteins (pink). Top right (E): Control simulation (DNA+rib-only) with $\phi = 0.104$ for comparison to (D). The chromosome is coarse-grained at 100 bp per bead (see *Methods*); cytoplasmic proteins are modeled as monodisperse spheres with an effective size based on Breuer et al. [79].

<https://doi.org/10.1371/journal.pcbi.1013898.g006>

This size dependence is consistent with an entropy-driven partitioning mechanism: smaller proteins can occupy nucleoid pores, increasing local packing while maintaining substantial short-range (in-cage) motion, whereas larger ribosomes gain more long-range configurational entropy by residing in the DNA-poor periphery [90]. This points to mechanisms beyond a simple volume-fraction increase, involving a competition between entropic effects across species and the enthalpic cost of deforming the DNA polymer (stretching and bending). Here we use “vibrational (short-range) entropy” to describe local in-cage motion within pores and “configurational (long-range) entropy” to describe large-scale rearrangements and sampling of many cages, consistent with the configurational–vibrational entropy separation in statistical mechanics [91,92]. Additional simulations support this preferential partitioning and its interplay with heterogeneous mesh size (see Fig D in S1 Text): as crowding increases, proteins shift toward larger pores near the nucleoid periphery and the DNA-depleted annulus widens, with the nucleoid compacting until balanced by the DNA’s elastic energy.

Overall, adding physiologically abundant (but charge-neutral) cytoplasmic proteins drives *more* nucleoid compaction and ribosome expulsion than in the DNA–ribosome-only model. Thus, any apparent ribosome interpenetration in DNA–ribosome-only models is contingent on an incomplete cytoplasmic composition: once protein crowdors are included at physiological abundance, excluded-volume interactions favor a size-dependent partitioning in which smaller proteins populate nucleoid pores while larger ribosomes redistribute toward the DNA-poor periphery. In this physiological mixture, excluded-volume interactions favor compaction rather than a stable, cell-spanning nucleoid. Because proteins, ribosomes, and DNA are charged macromolecules, we next examine how electrostatic interactions reshape these distributions.

Effect of electrostatic interactions in nucleoid compaction and organization of cytoplasm

Notably, nearly 75% of Syn3A proteins are positively charged, with the remaining 25% negatively charged. In *E. coli*, this balance is essentially flipped: about 40% of proteins are positively charged and 60% are negatively charged. We therefore suspect that Syn3A’s unusual proteome charge distribution may influence nucleoid expansion.

To probe how electrostatics shapes molecular organization in Syn3A, we assigned each biomolecule an electrostatic surface charge (see *Methods*). For all species, we incorporated the effect of Manning counterion-condensation (Eq 7) to obtain effective charges (see *Methods*). For DNA and ribosomes, we applied uniformly distributed negative surface charge densities using experimentally determined values, either from direct measurements or inferred from structure [93, 94]. Because each DNA bead represents 100 bp with radius 6 nm, we accounted for coiling over this length scale by converting DNA’s linear charge density (5.9 e/nm) into a bead charge: over a 12 nm diameter this corresponds to $-70 e$ per 100 bp (i.e., $-0.7 e/\text{bp}$).

For proteins, we inferred surface charge from structural data [79]. We coarse-grained the resulting patchy, pH-dependent residue-level charge patterns onto our single-bead protein representation by assigning each protein its mean surface charge (see Fig Ab in S1 Text). To isolate the qualitative effect of the proteome-wide charge distribution, we further grouped proteins by net sign and assigned group-average charges of $+10 e$ (positively charged proteins) and $-7 e$ (negatively charged proteins). The mean protein size (3 nm) was taken from the same source.

Electrostatic interaction range was encoded through the Debye length, κ^{-1} , in the Debye–Hückel interaction potential (see *Methods*); we tested $\kappa^{-1} = 2.2, 1.02, \text{ and } 0.68 \text{ nm}$ (discussed below). Membrane-bound proteins were not included in the model.

Fig 7 shows the equilibrated distributions of DNA, ribosomes, and proteins in the Syn3A model cell. The snapshot in Fig 7A provides a qualitative view of molecular organization; in the right half of the image, we highlight nucleoid morphology by rendering a subset of molecules invisible. Visually, the nucleoid spans most of the cell, and (negatively charged) ribosomes are abundant deep within the (negatively charged) nucleoid. This is counterintuitive, given the ribosome’s strong negative charge, which should electrostatically repel DNA and thus bias ribosomes away from the nucleoid.

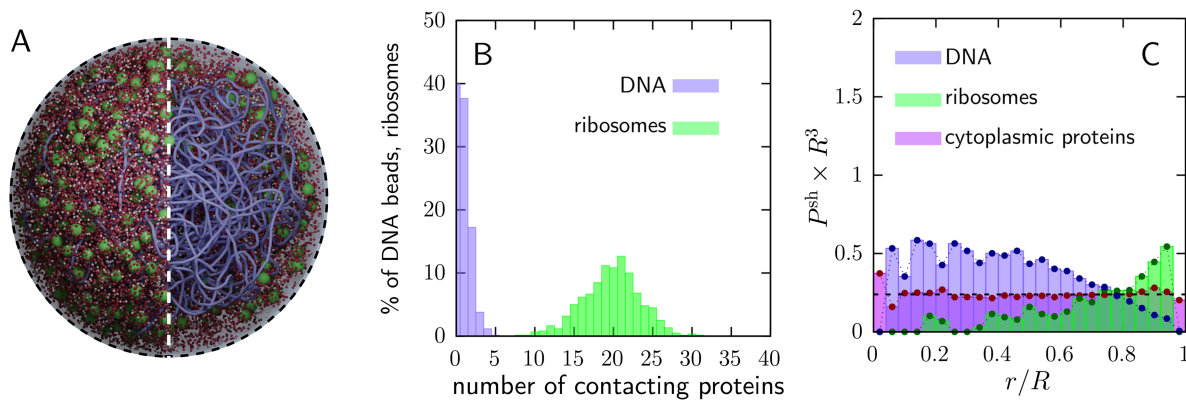


Fig 7. Influence of electrostatic interactions on nucleoid and cytoplasmic organization in the JCVI-Syn3A model cell. Electrostatic interactions among DNA, ribosomes, and proteins are defined in *Methods*. Results shown use Debye length $\kappa^{-1} = 0.68$ nm, DNA charge $q_{\text{DNA}} = -70 e$ per bead, protein charges $q_{\text{prot},+} = +10 e$ and $q_{\text{prot},-} = -7 e$, and ribosome charge $q_{\text{rib}} = -4000 e$. All interactions adjusted for Manning counterion condensation as indicated in text. (A) Equilibrated whole-cell snapshot showing DNA (purple), ribosomes (green), positively charged proteins (red), and negatively charged proteins (white). (B) Fraction of DNA beads and ribosomes coated by N proteins (horizontal axis), averaged over all DNA beads or all ribosomes and over the time window $16a_{\text{DNA}}^2/D$, where $D = kT/(6\pi\eta a_{\text{DNA}})$. Data from a single simulation. (C) Radial distributions of DNA (purple), ribosomes (green), and proteins (pink).

<https://doi.org/10.1371/journal.pcbi.1013898.g007>

One possible explanation is suggested by the protein enrichment around both DNA beads and ribosomes, visible in the snapshot and quantified in Fig H in *S1 Text*. We speculate that transient protein clustering around ribosomes partially screens ribosome–DNA electrostatic repulsion, enabling ribosomes to interpenetrate the nucleoid. Syn3A’s high abundance of positively charged proteins would further promote this effect.

To quantify this putative shielding effect, we computed the number of proteins electrostatically associated with each ribosome and averaged this quantity over all ribosomes and over a window of several Brownian times, $16a_{\text{DNA}}^2/D$, where $D = kT/(6\pi\eta a_{\text{DNA}})$. We repeated the same analysis for DNA beads and report the resulting distributions in Fig 7B. The ribosome–protein enrichment should be interpreted as dynamic, electrostatically mediated recruitment rather than formation of long-lived, stoichiometric complexes.

Over this interval—long enough for a ribosome to migrate within the nucleoid—approximately 50% of ribosomes have 15–25 proteins associated with their surface. This enrichment of surrounding, positively charged proteins is expected to partially screen the ribosome’s strong negative charge. We hypothesize that such “charge shielding” explains why, in the charged model, approximately 59.3% of ribosomes dynamically reside within the nucleoid (defined here as the region enclosing 90% of the DNA) in Fig 7C, compared with 36.2% in the charge-neutral model. The resulting ribosome distribution is consistent with experimental observations in Syn3A [34] and in several *Mycoplasma* species [32,33,35].

Concomitantly, the nucleoid expands to occupy a larger fraction of the cell volume. Together, these results suggest that electrostatic shielding can drive a cell-wide ribosome distribution in Syn3A and may contribute to similar organization in other *Mycoplasmas*. They are also consistent with recent measurements in *E. coli* linking ribosome migration to coating by positively charged proteins [8,95], although the effect is expected to be weaker in *E. coli* given its lower positively charged protein-to-ribosome ratio (60:1 in *E. coli* [calculated based on data from [96]] versus 120:1 in Syn3A).

Electrostatic repulsion between ribosomes and DNA can also be reduced when positively charged proteins condense onto DNA, effectively lowering the local negative charge experienced by nearby ribosomes. We found that 8% of positively charged proteins are condensed onto DNA, defined here as residing within 10% of the combined particle radii, i.e., at separations $< 1.1 (a_{\text{DNA}} + a_{\text{prot}})$. In contrast, negatively charged proteins show no enrichment near ribosomes beyond what is expected from Brownian diffusion.

Throughout, we use “charge shielding” to denote a reduction in the effective *short-range* electrostatic interactions between macromolecules due to nearby oppositely charged proteins. This is distinct from ionic screening, which is already encoded in the Debye–Hückel interaction via the Debye length (see *Methods*). A detailed sensitivity analysis of ionic screening and biomolecular charge, and their influence on biomolecular distributions via charge shielding, is provided in the [S1 Text](#).

In summary, the high abundance of positively charged proteins promotes charge shielding of ribosomes, enabling them to interpenetrate the nucleoid and thereby increasing the nucleoid’s tendency to expand throughout the cell. Concomitantly, several thousand DNA beads redistribute from the cell center into an annular region near the membrane (although this shift is visually subtle in [Fig 7C](#) because the annulus occupies a substantially larger volume). The resulting organization is consistent with experimental measurements of ribosome distributions in Syn3A [34,70] and with reports of expanded nucleoids in some *Mycoplasma* species [29–31].

Discussion and concluding remarks

Nucleoid compaction in bacterial cells is commonly attributed to DNA supercoiling, bridging by nucleoid-associated proteins (NAPs), and cytoplasmic crowding [12,22,27,41]. In many bacteria, including *Escherichia coli*, these mechanisms confine the nucleoid to a central subcellular volume. In contrast, many *Mycoplasma*—including the *Mycoplasma*-derived synthetic minimal cell JCVI-Syn3A—exhibit a cell-spanning nucleoid. This expanded-nucleoid state has been attributed to reduced levels of NAPs and other supercoiling-active proteins. Concomitantly, ribosome organization differs markedly between compacted- and expanded-nucleoid cells: ribosomes are concentrated outside the nucleoid in the former, but are distributed throughout the nucleoid (and cell) in the latter. This coupling between genome-encoded composition, physical organization, and cellular function motivates us to define ‘physiotype’ to denote a physical intermediate between genotype and phenotype. In a genotype-to-‘physiotype’-to-phenotype perspective, spatial organization shapes the opportunity for coupled transcription and translation [5], with downstream phenotypic consequences.

Recent experiments on Syn3A reported an approximately uniform ribosome distribution throughout the cell [34], motivating computational reconstructions in which ribosomes are placed according to experiment and a nucleoid self-assembles in the remaining space [70]. Syn3A is an especially well-controlled system for interrogating an expanded-nucleoid physiotype: it has a minimal genome and proteome, and its NAP complement is limited to a single type (HU). Recent discussions (personal communication, John I. Glass, J. Craig Venter Inst.) therefore raised a natural hypothesis that HU paucity is the primary driver of Syn3A’s cell-spanning nucleoid and uniform ribosome distribution. However, prior Syn3A models treated DNA and ribosomes alone and assumed charge-neutral macromolecules [70,77], motivating a more physically complete model.

We developed a Brownian dynamics model of Syn3A and reproduced the experimentally reported ribosome distribution used in prior work [34,70,77]. Using a swelling Monte Carlo algorithm [97,98], we generated an initial, self-assembled nucleoid under the same charge-neutral assumptions. Upon initiation of Brownian dynamics, however, this initialized configuration is lost: the experimentally consistent initial condition (DNA and ribosomes only, with no other proteins and no charges) is dynamically unstable, and ribosomes rapidly redistribute toward the cell periphery. This heterogeneous ribosome population is inconsistent with experiments, pointing to missing physics and motivating the refined model developed here.

We first asked whether “standard” compaction mechanisms could explain Syn3A’s cell-spanning nucleoid. Incorporating physiological DNA stiffness and HU-mediated remodeling of nucleoid microstructure (via HU binding and induced bends) consistently drove the system toward *greater* compaction, not expansion. These mechanical effects were further amplified by cytoplasmic crowding: when we added charge-neutral cytoplasmic proteins at literature-based abundance and packing fraction, the explicit excluded-volume of the proteome—absent from prior Syn3A models—*exacerbated* ribosome expulsion and nucleoid compaction once dynamics were allowed. In other words, had earlier models included the

physical presence of proteins and Brownian motion, they would have robustly revealed compaction as the default outcome. The qualitative behavior reverses *only* when we include the missing ingredient: electrostatics. Endowing the proteome with a physiological distribution of electrostatic charge produces a stable, expanded nucleoid and restores a near-uniform ribosome distribution.

These results sharpen the mechanistic picture: DNA stiffness, HU-induced bending, and protein crowding all favor nucleoid compaction, whereas electrostatic interactions are the only mechanism we studied that counteracts this trend and stabilizes Syn3A's expanded-nucleoid physiotype. The key is Syn3A's atypical proteomic charge composition—a proteome dominated by positively charged proteins, with an unusually high ratio of positively charged proteins per ribosome (approximately doubled relative to *E. coli*). In the charged model, positively charged proteins dynamically enrich around ribosomes and DNA, and we *quantified* the resulting “charge shielding” by measuring (i) the distribution of protein association numbers around ribosomes and DNA beads and (ii) the corresponding redistribution of ribosomes and DNA across the cell volume. Consistent with this picture, ribosomes become substantially more prevalent within the nucleoid once charges are included, supporting the hypothesis that protein-mediated shielding reduces effective ribosome–DNA repulsion and allows ribosomes to interpenetrate and expand the nucleoid [8].

Our traversability analysis highlights that nucleoid mesh geometry can, in principle, constrain macromolecular transport and promote trapping within the nucleoid, even at comparable overall DNA compaction. This provides a quantitative tool for probing accessibility of genomic regions and potential links to translation organization, including proposed polysome formation deep within *E. coli*'s nucleoid [2,86]. Here we applied the analysis to an ensemble of nascent (pre-replication) configurations; extending it across growth conditions and cell-cycle stages is a natural next step.

Several extensions would help refine the mechanistic picture of electrostatically driven clustering and nucleoid organization. In the present model, protein electrostatics are intentionally coarse-grained: protein surface charge is treated as isotropic, with a single representative charge for all positively charged proteins and a second for all negatively charged proteins, and proteins are assigned a single mean size. A natural next step is to incorporate more detailed proteome heterogeneity, including distributions of protein charge and size, anisotropic (patchy) surface charge, and environmental dependence through pH and salt (Debye length), all of which can influence clustering and nucleoid organization. These refinements are particularly relevant for predictive modeling and engineering of synthetic cells. Ribosomes can also form polysomes, which can affect bacterial spatial organization [8]; incorporating explicit polysomes (rather than independent ribosomes) is therefore an important direction for future work.

The methods and frameworks developed here can be extended to incorporate additional molecular detail—including richer proteomic heterogeneity and explicit representations of mRNA translation [10,11] and transcription—and then applied to other bacterial systems.

Our framework is generalizable along two axes: the interaction physics included and the organism/cell instantiated. The pipeline that maps PDB-derived structure to coarse-grained protein size and charge can naturally be extended to include patchy surface charge and physiological size polydispersity across diverse cellular environments [11]. Likewise, the full-cell model can be parameterized from proteomics data for any bacterium where such data exist, and our genome-construction approach scales to long chromosomes (e.g., *E. coli* at 10 bp resolution). More detailed, sequence-specific biochemistry—including protein–DNA binding, supercoiling, and dynamic winding/unwinding—can be layered onto the same mesoscale scaffold to address organism-specific regulation and nucleoid accessibility.

Beyond natural bacteria, this framework is well suited for synthetic-cell design. By prescribing compartment geometry and composition, one can input custom proteomes and gene sets and predict how engineered constituents reshape nucleoid organization and the accessibility of targeted chromosomal regions. This opens a route to rationally tuning genome compaction and expression capacity—for example, by engineering proteome charge balance to modulate nucleoid expansion, or by organizing translation components into DNA-depleted zones to create high-yield “expression factories.” While such applications will require system-specific parameterization, the underlying pipeline provides a versatile, extensible bridge from genotype to physiotype to phenotype.

Finally, our results emphasize how effective electrostatics, even when modeled implicitly, interact with crowding to shape genome-scale organization. Coupled with ion-explicit molecular dynamics, this framework can guide the design of synthetic or cell-free systems by informing choices of crowding agents and ionic conditions that better recapitulate *in vivo* behavior.

Methods

Intermolecular interactions

Proteins, ribosomes, and DNA beads are represented as interacting spheres suspended in a Newtonian cytosol, consistent with recent whole-cell coarse-grained models [8,70,99]. Nonbonded interactions comprise excluded-volume repulsion and (when enabled) screened electrostatics. Hard-sphere exclusion between particles i and j is

$$V_{ij}^{HS}(\mathbf{r}_i, \mathbf{r}_j) = \begin{cases} 0 & \text{if } r_{ij} > a_i + a_j \\ \infty & \text{if } r_{ij} \leq a_i + a_j \end{cases}, \quad (2)$$

where $r_{ij} = \|\mathbf{r}_i - \mathbf{r}_j\|$ is the distance between the two beads i and j centered at \mathbf{r}_i and \mathbf{r}_j with radii a_i and a_j . A similar interaction potential is also used to model interactions between macromolecules and the cell membrane. In our *Brownian* simulations, V_{ij}^{HS} is replaced by a steep, nearly hard repulsive Morse potential,

$$V_{ij}^{\text{morse}}(\mathbf{r}_i, \mathbf{r}_j) = \begin{cases} 0 & \text{if } r_{ij} > a_i + a_j \\ (6kT(1 - \exp(-60(r_{ij} - a_i - a_j)/a_{\text{DNA}})))^2 & \text{if } r_{ij} \leq a_i + a_j \end{cases}, \quad (3)$$

where k is Boltzmann's constant and T is the absolute temperature. The potential in Eq (3) has been shown to recover hard-sphere behavior for volume fractions up to 50% [100,101].

We modeled the circular bacterial chromosome as a closed-loop bead-spring polymer chain, consistent with previous DNA modeling approaches [82,102]. The beads interact with each other via electrostatic attraction and repulsion, as well as hard-sphere exclusion, and also spring-like forces between base pairs and beads. The resistance to stretching and bending of the coarse-grained DNA chain is governed by spring and bending harmonic potentials, given, respectively, by

$$V_{ij}^s(\mathbf{r}_i, \mathbf{r}_j) = kT \frac{\sigma_s}{2\ell_0^2} (r_{ij} - \ell_0)^2, \quad (4)$$

$$\text{and} \quad V_i^b = kT \frac{\sigma_b}{2} (\theta_i - \theta_i^0)^2, \quad (5)$$

where ℓ_0 is the equilibrium bond length between a pair of adjacent DNA beads. In Eq (5), θ_i is the angle formed by a triplet of beads consisting of the DNA bead i and its neighbors, and θ_i^0 is the triplet's equilibrium angle (described in next section). The dimensionless coefficients σ_s and σ_b are the *stretching stiffness* and *bending stiffness*, respectively. For "bare" DNA (i.e., in the absence of NAPs binding to DNA), the equilibrium angle $\theta_j^0 = \pi$ for all triplets throughout the entire chain. However, this equilibrium angle can be locally changed upon binding of bend-inducing HU proteins to the DNA [see Fig 5 and corresponding discussion].

Electrostatic interactions are modeled by a Debye–Hückel potential between particles with nominal charges q_i and q_j (see S1 Text for charge determination),

$$V_{ij}^{\text{elec}} = kT \frac{A_{ij}}{\kappa r} \exp(-\kappa(r_{ij} - a_i - a_j)), \quad (6)$$

where A_{ij} is related to the net surface charges of particles i and j by [8,94]

$$A_{ij} = A_i A_j, \text{ where } A_i = \text{sign}(q_i) \sqrt{\frac{3}{4} q_{i,\text{eff}}}, \quad (7)$$

where $q_{i,\text{eff}} = 0.6\sqrt{|q_i|} \log(|q_i|/2 + 1)$ is the effective charge of the i -th particle and κ^{-1} is the Debye length. This effective-charge mapping, introduced by Dutagaci et al. [94], provides a computationally efficient way to incorporate charge renormalization. Its sublinear dependence on $|q_i|$ mimics counterion-condensation (Manning-type) attenuation without explicitly simulating bound counterions.

Bare charges used to compute $q_{i,\text{eff}}$ are summarized in Table 1. Ribosome charge is adopted from Dutagaci et al. [94]. Cytoplasmic proteins are assigned class-average charges computed from the JCVI-Syn3A proteome (Fig A in S1 Text): $q_{\text{prot},+} = +10 e$ and $q_{\text{prot},-} = -7 e$. Each DNA bead represents a locally compacted 100-bp segment and is modeled as a sphere of radius 6 nm. Assigning the full phosphate charge of 100 bp ($\sim -200 e$) to a 6 nm bead would unrealistically increase the local line-charge density. Instead, we assign each DNA bead the bare charge associated with a 12 nm backbone segment using DNA's linear charge density ($-5.9 e/\text{nm}$), yielding $\sim -70 e$ per bead, and then apply the effective-charge mapping in Eq (7).

To assess sensitivity, we also examined two larger DNA bare-charge values in the S1 Text: (i) $-200 e$, corresponding to assigning the full phosphate charge of 100 bp (straight-backbone assumption), and (ii) $-400 e$, an upper-bound obtained by projecting an experimentally reported DNA surface charge density onto an equivalent total charge for a 6 nm spherical bead. These values are used to span electrostatic strengths rather than as equally physical representations.

Following Wennerström et al. [103], selective ion partitioning and macromolecular electroneutrality can increase the effective cytosolic Debye length; we therefore treat $\kappa^{-1} \approx 2.2 \text{ nm}$ as a plausible upper bound. As a lower bound, we compute κ^{-1} for a representative monovalent ionic strength $I = 0.2 \text{ M}$ using the standard Debye-Hückel expression

$$\kappa^{-1} = \sqrt{\frac{\epsilon_0 \epsilon_r kT}{2N_A I e^2}}, \quad (8)$$

we get $\kappa^{-1} \approx 0.68 \text{ nm}$. Here, ϵ_0 is the permittivity of free space, ϵ_r is the dielectric constant, N_A is the Avagadro number, and e is the electronic charge. Sensitivity of biomolecular organization across this range is examined in the S1 Text (Figs G and H in S1 Text). We have tabulated all the fixed parameters used in our JCVI-Syn3A model in Table 1.

Table 1. Fixed parameters used in the Syn3A model. Values obtained through the pipeline in Fig A in S1 Text using data from Refs [79,93,94].

Quantity	Value	Notes	Source
Cell radius, R	225 nm	Standard; 201 nm in Fig 1	[70,79]
Stretching stiffness, σ_s	1	Dimensionless	[82]
Ribosome count	600	Standard; 503 in Fig 1	[70,79]
Protein radius, a_{prot}	3 nm		Fig A in S1 Text
Ribosome radius, a_{rib}	13 nm		[94]
DNA bead radius, a_{DNA}	6 nm	100 bp/bead	[82]
Debye length, κ^{-1}	0.68 nm	Fig 7; also 1.02 nm and 2.2 nm (Figs G and H in S1 Text)	[103]
DNA bead charge, q_{DNA}	$-70 e$	Fig 7; also $-200 e$ and $-400 e$ (Figs G and H in S1 Text)	[93]
Protein charge, $q_{\text{prot},+}$	$+10 e$	Positively charged proteins	Fig A in S1 Text
Protein charge, $q_{\text{prot},-}$	$-7 e$	Negatively charged proteins	Fig A in S1 Text
Ribosome charge, q_{rib}	$-4 \times 10^3 e$		[94]

<https://doi.org/10.1371/journal.pcbi.1013898.t001>

Swelling Monte Carlo algorithm

To generate the macromolecular distributions of ribosomes, proteins, and the chromosome in Syn3A, we use an extension of the swelling Monte Carlo algorithm developed in [97,104]. The method is illustrated in Fig 8. We initialize all macromolecules' center positions in a uniform spatial distribution throughout the cell [Fig 8A]. We then apply alternating Monte Carlo translation and swelling moves to each particle to resolve overlaps [Fig 8B], to a physically consistent, dense configuration at the target packing fraction [Fig 8C]. The DNA is simultaneously self-assembled as it and the ribosomes take on their finite-size positions. Fig 8D illustrates the 100bp/bead coarse graining (top) and the stretching and bending potentials between DNA beads (bottom). Full algorithmic details, including parameter choices and convergence criteria, are provided in S1 Text.

Unlike approaches that prescribe macromolecular placement—for example, the Koch-curve chromosome construction used in [70]—this method does not require prior knowledge of experimentally measured macromolecular positions. Instead, macromolecular organization emerges from the specified physical interactions.

Langevin dynamics

For our mesoscale dynamic simulations, the motion of the coarse-grained macromolecules in the cell is governed by Newton's second law, resulting in a Langevin equation:

$$m \cdot \frac{d\mathbf{U}}{dt} = \mathbf{F}^H + \mathbf{F}^P + \mathbf{F}^B, \quad (9)$$

where m is a diagonal mass matrix, \mathbf{U} is the velocity of all particles, \mathbf{F}^P are the forces due to interparticle and particle-membrane interactions, given by

$$\mathbf{F}_i^P = -\nabla_{\mathbf{r}_i} V, \quad (10)$$

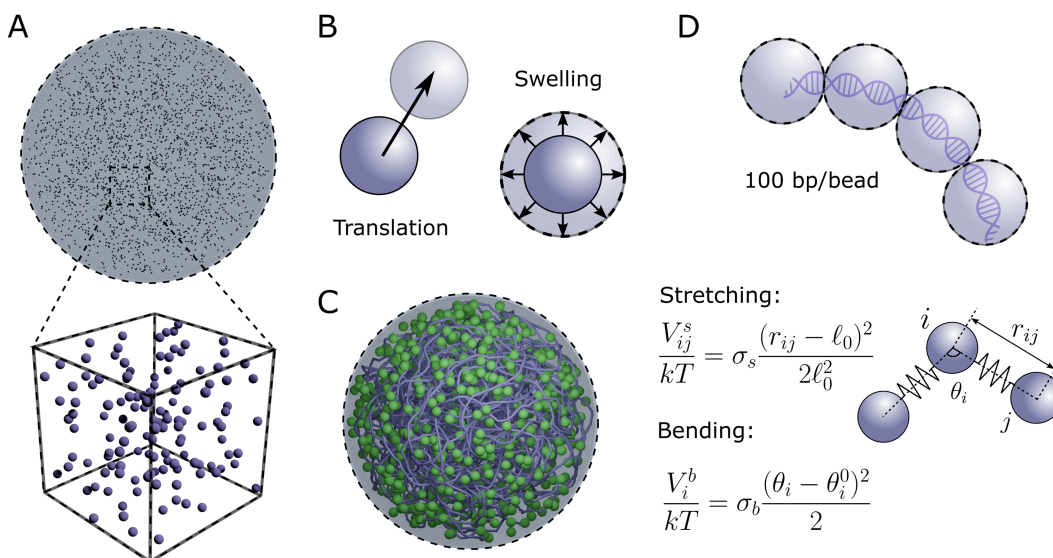


Fig 8. Illustration of the swelling Monte Carlo algorithm used to generate whole-cell configurations. (A) Macromolecules are initialized as point particles uniformly distributed throughout the cell and labeled by type (which determines their size and interaction potentials). (B) Particles then undergo two Monte Carlo moves: translation and swelling. (C) Resulting equilibrated whole-cell configuration. The chromosome is shown as a continuous backbone. (D) DNA beads (100 bp per bead, top) are connected through bead-spring and bending interactions (bottom), Eqs (4) and (5).

<https://doi.org/10.1371/journal.pcbi.1013898.g008>

where

$$V = \sum_{ij} (V_{ij}^{\text{morse}} + V_{ij}^{\text{s}} + V_{ij}^{\text{elec}}) + \sum_i V_i^b \quad (11)$$

is the total potential energy of the system. Moreover, \mathbf{F}^H are the hydrodynamic forces, which, for spheres in the freely draining limit and in the absence of an external flow, are given by Stokes' law $\mathbf{F}^H = -6\pi\eta\mathbf{a} \cdot \mathbf{U}$, where \mathbf{a} is a diagonal particle-radius matrix. Lastly, \mathbf{F}^B are the random forces and torques due to Brownian motion, given by $\mathbf{F}^B = \mathbf{A} \cdot \Psi$, where \mathbf{A} is a positive-definite symmetric matrix and $\Psi(t)$ is a white noise stochastic process, related to the hydrodynamic forces by the fluctuation-dissipation theorem.

$$\langle \Psi \rangle = 0, \quad (12)$$

$$\langle \Psi(t_0)\Psi(t_0 + t) \rangle = \delta(t)\mathbf{I}, \quad (13)$$

$$\text{and } \mathbf{A}^2 = 2kT(6\pi\eta\mathbf{a}), \quad (14)$$

where \mathbf{I} is the identity matrix, and $\delta(t)$ is the Dirac delta distribution. Eq (9) is numerically integrated using the `langevin` integrator in LAMMPS for a Stokes number $St = 10^{-4}$, chosen to approach the overdamped limit of the Langevin equation. Similar to [8], the timestep was chosen to be 42 ps. Interactions between the macromolecules and the cell membrane are modeled similar to [8] by adding an additional force to Eq (9) that act inward in the radial direction given by $\mathbf{F}^W = -K(r_i - R - a_i)^2 \hat{\mathbf{e}}_r$ for $r_i = ||\mathbf{r}_i|| \geq R - a_i$ and $\hat{\mathbf{e}}_r = \mathbf{r}_i/r_i$.

In our mesoscale simulations, we first equilibrated the initial distributions of DNA, ribosomes, and proteins in the absence of electrostatic interactions (Fig 6). We then enabled electrostatics, after which particles evolved under Brownian motion according to the Langevin dynamics in Eq (9), interacting via both excluded-volume (entropic) and charge-mediated forces.

Radial distribution function for single and multiple realizations

To quantify the distribution of DNA and ribosomes throughout the cell, we introduce reduced probability densities $P(r)$ for each particle type. Due to radial symmetry, the true ensemble distribution only depends on the radial coordinate $r = ||\mathbf{r}||$ and we write $P(r)$. For a single numerical realization, the particle configuration is known and the probability density is given by

$$P(r) = \frac{1}{N} \sum_{k=1}^N \delta(r - r_k), \quad (15)$$

where N is the number of macromolecules of a given type and δ is the three-dimensional Dirac delta distribution. In this case, it is convenient to partition the cell domain into finite spherical shells of thickness h and calculate a shell-binned probability distribution, given by

$$P^{\text{sh}}(r) = \frac{1}{V_{\text{sh}}} \int_{V_{\text{sh}}} P(r) dV \quad (16)$$

This approach, similar to previous works in confined systems [7, 105], quantifies the fraction of macromolecules whose centers are located in a spherical shell of radius r and thickness h , normalized by the shell volume. For our results, we use $h = 2a_{\text{rib}}$. For a large number of particles $N \gg 1$ and small shell thickness h , this distribution approximates the real (ensemble) distribution function $P(r)$.

For multiple runs, as we have many more available data points, the ensemble probability distribution $P(r)$ can be better approximated by using spectral-decomposition methods [106]. To do so, we decompose $P(r)$ in a series of orthonormal functions ϕ_n as $P(r) = \sum_n c_n \phi_n(r)$. The coefficients c_n can be calculated via orthogonal projection as:

$$c_n = \langle P, \phi_n \rangle = \int_0^R P(r) \phi_n(r) w(r) dr = \left\langle \frac{\phi_n(r) w(r)}{4\pi r^2} \right\rangle, \quad (17)$$

where $w(r)$ is the inner product weight and the angle brackets denote an ensemble average. For numerical purposes, we truncate the Fourier series at a finite number of basis functions. To calculate the coefficients c_n , we use a Monte Carlo quadrature to approximate the ensemble average in Eq (17) by an arithmetic over multiple particles at multiple runs, as in the methodology proposed in [106]. More specifically, we use the even Chebyshev polynomials as basis functions when expanding $P(r)$, for which $w(r) \propto 1/\sqrt{1-x^2}$.

Calculation of average penetration length and traversability

The average penetration length $\langle L_p \rangle$ shown in Fig 4 is defined as

$$\langle L_p \rangle = \sum_k L_p(V_k) P_k, \quad (18)$$

where the summation is performed over all connected components of the Voronoi network for a particle of size a . $P_k(a)$ is the probability of a particle of such size being in the traversable region defined by the k -th connected component of the Voronoi network $V_k(a)$. As the Voronoi network provides a good representation of the accessible regions for a given particle of size a , we make a simplifying assumption that there is an equal likelihood of a particle to be in any of the accessible Voronoi edges, meaning that P_k is given by $N_e^k(a)/N_e(a)$, where $N_e^k(a)$ is the number of edges in $V_k(a)$ and $N_e(a)$ is the total number of Voronoi voids traversable by a particle of size a . Similarly, the traversability $\text{Tv}(\alpha)$, shown in Fig 4C, is defined as the probability of a particle being able to traverse a radial length α inside the cell. In Fig 4C, $\alpha = R_{95}$. Mathematically, this is given by

$$\text{Tv}(\alpha) = \mathbb{P}\{L_p(V_k) \geq \alpha\} = \sum_k K(V_k, \alpha) P_k, \quad (19)$$

where the indicator function K is given by

$$K(V_k, \alpha) = \begin{cases} 0 & \text{if } L_p(V_k) < \alpha \\ 1 & \text{if } L_p(V_k) \geq \alpha. \end{cases} \quad (20)$$

Cluster size calculation

Cluster sizes in Fig H in S1 Text are computed using a graph-based (connected-components) algorithm, analogous to that used in our traversability analysis. We define an undirected contact network in which nodes represent beads and an edge connects particles i and j when their center-to-center separation satisfies $r_{ij} < c_{ij}$, $c_{ij} = 1.1(a_i + a_j)$, where a_i and a_j are the bead radii.

Supporting information

S1 Text. Supplementary material and results.

(PDF)

Acknowledgments

We acknowledge computational support of the University of Missouri Hellbender High Performance Computer Cluster (RNZ, VSS, GR). The authors thank Dr. John Glass (JCVI) for providing genomic data, the suggestion that HU proteins underlie Syn3A's expanded nucleoid, and many useful conversations. We also gratefully acknowledge many insightful conversations with Dr. Kate Adamala (University of Minnesota), which expanded our vision of the work. The authors also thank the Build-A-Cell and SynCell communities for providing a robust community for exchange of ideas.

Author contributions

Conceptualization: Gesse Roure, Vishal S. Sivasankar, Roseanna N. Zia.

Data curation: Gesse Roure, Vishal S. Sivasankar.

Formal analysis: Gesse Roure, Vishal S. Sivasankar, Roseanna N. Zia.

Funding acquisition: Roseanna N. Zia.

Investigation: Gesse Roure, Vishal S. Sivasankar, Roseanna N. Zia.

Methodology: Gesse Roure, Vishal S. Sivasankar, Roseanna N. Zia.

Project administration: Roseanna N. Zia.

Resources: Roseanna N. Zia.

Software: Gesse Roure.

Supervision: Roseanna N. Zia.

Validation: Gesse Roure, Roseanna N. Zia.

Visualization: Gesse Roure.

Writing – original draft: Gesse Roure, Vishal S. Sivasankar, Roseanna N. Zia.

Writing – review & editing: Gesse Roure, Vishal S. Sivasankar, Roseanna N. Zia.

References

1. Valkenburg JA, Woldringh CL. Phase separation between nucleoid and cytoplasm in *Escherichia coli* as defined by immersive refractometry. *J Bacteriol.* 1984;160(3):1151–7. <https://doi.org/10.1128/jb.160.3.1151-1157.1984> PMID: 6389508
2. Gray WT, Govers SK, Xiang Y, Parry BR, Campos M, Kim S, et al. Nucleoid size scaling and intracellular organization of translation across bacteria. *Cell.* 2019;177(6):1632–1648.e20. <https://doi.org/10.1016/j.cell.2019.05.017> PMID: 31150626
3. Mondal J, Bratton BP, Li Y, Yethiraj A, Weisshaar JC. Entropy-based mechanism of ribosome-nucleoid segregation in *E. coli* cells. *Biophys J.* 2011;100(11):2605–13. <https://doi.org/10.1016/j.bpj.2011.04.030> PMID: 21641305
4. Kim J, Jeon C, Jeong H, Jung Y, Ha B-Y. A polymer in a crowded and confined space: effects of crowder size and poly-dispersity. *Soft Matter.* 2015;11(10):1877–88. <https://doi.org/10.1039/c4sm02198c> PMID: 25535704
5. Dersch S, Rotter DAO, Graumann PL. Heterogeneity of subcellular diffusion in bacteria based on spatial segregation of ribosomes and nucleoids. *Microb Physiol.* 2022;32(5–6):177–86. <https://doi.org/10.1159/000526846> PMID: 36070705
6. Bakshi S, Siryaporn A, Goulian M, Weisshaar JC. Superresolution imaging of ribosomes and RNA polymerase in live *Escherichia coli* cells. *Mol Microbiol.* 2012;85(1):21–38. <https://doi.org/10.1111/j.1365-2958.2012.08081.x> PMID: 22624875
7. Aponte-Rivera C, Zia RN. Simulation of hydrodynamically interacting particles confined by a spherical cavity. *Phys Rev Fluids.* 2016;1(2). <https://doi.org/10.1103/physrevfluids.1.023301>
8. Valverde-Mendez D, Sunol AM, Bratton BP, Delarue M, Hofmann JL, Sheehan JP. Macromolecular interactions and geometrical confinement determine the 3D diffusion of ribosome-sized particles in live *Escherichia coli* cells. *bioRxiv.* 2024;:2024–03.
9. Rissland OS. The organization and regulation of mRNA-protein complexes. *Wiley Interdiscip Rev RNA.* 2017;8(1):e1369. <https://doi.org/10.1002/wrna.1369> PMID: 27324829

10. Maheshwari AJ, Sunol AM, Gonzalez E, Endy D, Zia RN. Colloidal physics modeling reveals how per-ribosome productivity increases with growth rate in *Escherichia coli*. *mBio*. 2023;14(1):e0286522. <https://doi.org/10.1128/mbio.02865-22> PMID: 36537810
11. Hofmann JL, Yang TS, Sunol AM, Zia RN. Ribosomal L12 stalks recruit elongation factors to speed protein synthesis in *Escherichia coli*. *Commun Biol*. 2025;8(1):940. <https://doi.org/10.1038/s42003-025-08366-4> PMID: 40537567
12. Murphy LD, Zimmerman SB. Condensation and cohesion of lambda DNA in cell extracts and other media: implications for the structure and function of DNA in prokaryotes. *Biophys Chem*. 1995;57(1):71–92. [https://doi.org/10.1016/0301-4622\(95\)00047-2](https://doi.org/10.1016/0301-4622(95)00047-2) PMID: 8534838
13. Ramos JEB Jr, de Vries R, Ruggiero Neto J. DNA psi-condensation and reentrant decondensation: effect of the PEG degree of polymerization. *J Phys Chem B*. 2005;109(49):23661–5. <https://doi.org/10.1021/jp0527103> PMID: 16375345
14. Zhang C, Shao PG, van Kan JA, van der Maarel JRC. Macromolecular crowding induced elongation and compaction of single DNA molecules confined in a nanochannel. *Proc Natl Acad Sci U S A*. 2009;106(39):16651–6. <https://doi.org/10.1073/pnas.0904741106> PMID: 19805352
15. Yoshikawa K, Hirota S, Makita N, Yoshikawa Y. Compaction of DNA induced by like-charge protein: opposite salt-effect against the polymer-salt-induced condensation with neutral polymer. *J Phys Chem Lett*. 2010;1(12):1763–6. <https://doi.org/10.1021/jz100569e>
16. Krotova MK, Vasilevskaya VV, Makita N, Yoshikawa K, Khokhlov AR. DNA compaction in a crowded environment with negatively charged proteins. *Phys Rev Lett*. 2010;105(12):128302. <https://doi.org/10.1103/PhysRevLett.105.128302> PMID: 20867679
17. Pelletier J, Halvorsen K, Ha B-Y, Paparcone R, Sandler SJ, Woldringh CL, et al. Physical manipulation of the *Escherichia coli* chromosome reveals its soft nature. *Proc Natl Acad Sci U S A*. 2012;109(40):E2649–56. <https://doi.org/10.1073/pnas.1208689109> PMID: 22984156
18. Ojala H, Ziedaite G, Wallin AE, Bamford DH, Hæggröm E. Optical tweezers reveal force plateau and internal friction in PEG-induced DNA condensation. *Eur Biophys J*. 2014;43(2–3):71–9. <https://doi.org/10.1007/s00249-013-0941-x> PMID: 24477280
19. Mardoum WM, Gorczyca SM, Regan KE, Wu T-C, Robertson-Anderson RM. Crowding induces entropically-driven changes to DNA dynamics that depend on crowder structure and ionic conditions. *Front Phys*. 2018;6:53. <https://doi.org/10.3389/fphys.2018.00053> PMID: 31667164
20. Yang D, Männik J, Retterer ST, Männik J. The effects of polydisperse crowders on the compaction of the *Escherichia coli* nucleoid. *Mol Microbiol*. 2020;113(5):1022–37. <https://doi.org/10.1111/mmi.14467> PMID: 31961016
21. Collette D, Dunlap D, Finzi L. Macromolecular crowding and DNA: bridging the gap between in vitro and in vivo. *Int J Mol Sci*. 2023;24(24):17502. <https://doi.org/10.3390/ijms242417502> PMID: 38139331
22. Dillon SC, Dorman CJ. Bacterial nucleoid-associated proteins, nucleoid structure and gene expression. *Nat Rev Microbiol*. 2010;8(3):185–95. <https://doi.org/10.1038/nrmicro2261> PMID: 20140026
23. Dame RT. The role of nucleoid-associated proteins in the organization and compaction of bacterial chromatin. *Mol Microbiol*. 2005;56(4):858–70. <https://doi.org/10.1111/j.1365-2958.2005.04598.x> PMID: 15853876
24. Dahlke K, Sing CE. Influence of nucleoid-associated proteins on DNA supercoiling. *J Phys Chem B*. 2019;123(48):10152–62. <https://doi.org/10.1021/acs.jpcc.9b07436> PMID: 31710235
25. Gupta A, Wasim A, Mondal J. Nucleoid associated proteins and their effect on *E. coli* chromosome. *bioRxiv*. 2020::2020–11.
26. Winardhi RS, Yan J, Kenney LJ. H-NS regulates gene expression and compacts the nucleoid: insights from single-molecule experiments. *Biophys J*. 2015;109(7):1321–9. <https://doi.org/10.1016/j.bpj.2015.08.016> PMID: 26445432
27. Joyeux M. Organization of the bacterial nucleoid by DNA-bridging proteins and globular crowders. *Front Microbiol*. 2023;14:1116776. <https://doi.org/10.3389/fmicb.2023.1116776> PMID: 36925468
28. Seto S, Miyata M. Partitioning, movement, and positioning of nucleoids in *Mycoplasma capricolum*. *J Bacteriol*. 1999;181(19):6073–80. <https://doi.org/10.1128/JB.181.19.6073-6080.1999> PMID: 10498720
29. Seto S, Layh-Schmitt G, Kenri T, Miyata M. Visualization of the attachment organelle and cytoadherence proteins of *Mycoplasma pneumoniae* by immunofluorescence microscopy. *J Bacteriol*. 2001;183(5):1621–30. <https://doi.org/10.1128/JB.183.5.1621-1630.2001> PMID: 11160093
30. Trussart M, Yus E, Martinez S, Baù D, Tahara YO, Pengo T, et al. Defined chromosome structure in the genome-reduced bacterium *Mycoplasma pneumoniae*. *Nat Commun*. 2017;8:14665. <https://doi.org/10.1038/ncomms14665> PMID: 28272414
31. Martínez-Torró C, Torres-Puig S, Marcos-Silva M, Huguet-Ramón M, Muñoz-Navarro C, Lluch-Senar M. Functional characterization of the cell division gene cluster of the wall-less bacterium *Mycoplasma genitalium*. *Frontiers in Microbiology*. 2021;12:695572.
32. Kuhner S, van Noort V, Betts MJ, Leo-Macias A, Batisse C, Rode M, et al. Proteome organization in a genome-reduced bacterium. *Science*. 2009;326(5957):1235–40.
33. Scheffer MP, Gonzalez-Gonzalez L, Seybert A, Ratera M, Kunz M, Valpuesta JM, et al. Structural characterization of the NAP; the major adhesion complex of the human pathogen *Mycoplasma genitalium*. *Mol Microbiol*. 2017;105(6):869–79. <https://doi.org/10.1111/mmi.13743> PMID: 28671286
34. Gilbert BR, Thornburg ZR, Lam V, Rashid F-ZM, Glass JI, Villa E, et al. Generating chromosome geometries in a minimal cell from cryo-electron tomograms and chromosome conformation capture maps. *Front Mol Biosci*. 2021;8:644133. <https://doi.org/10.3389/fmolb.2021.644133> PMID: 34368224
35. Xue L, Lenz S, Zimmermann-Kogadeeva M, Tegunov D, Cramer P, Bork P, et al. Visualizing translation dynamics at atomic detail inside a bacterial cell. *Nature*. 2022;610(7930):205–11. <https://doi.org/10.1038/s41586-022-05255-2> PMID: 36171285
36. Wang M, Herrmann CJ, Simonovic M, Szklarczyk D, von Mering C. Version 4.0 of PaxDb: protein abundance data, integrated across model organisms, tissues, and cell-lines. *Proteomics*. 2015;15(18):3163–8. <https://doi.org/10.1002/pmic.201400441> PMID: 25656970

37. Kuzminov A. Bacterial nucleoid is a riddle wrapped in a mystery inside an enigma. *J Bacteriol.* 2024;206(3):e0021123. <https://doi.org/10.1128/jb.00211-23> PMID: 38358278
38. De Gennes PG. Collapse of a polymer chain in poor solvents. *J Physique Lett.* 1975;36(3):55–7. <https://doi.org/10.1051/jphyslet:0197500360305500>
39. Post CB, Zimm BH. Theory of DNA condensation: collapse versus aggregation. *Biopolymers.* 1982;21(11):2123–37. <https://doi.org/10.1002/bip.360211104> PMID: 7171729
40. de Vries R. Flexible polymer-induced condensation and bundle formation of DNA and F-actin filaments. *Biophys J.* 2001;80(3):1186–94. [https://doi.org/10.1016/S0006-3495\(01\)76095-X](https://doi.org/10.1016/S0006-3495(01)76095-X) PMID: 11222283
41. Odijk T. Osmotic compaction of supercoiled DNA into a bacterial nucleoid. *Biophys Chem.* 1998;73(1–2):23–9. [https://doi.org/10.1016/s0301-4622\(98\)00115-x](https://doi.org/10.1016/s0301-4622(98)00115-x) PMID: 9697298
42. Scolari VF, Cosentino Lagomarsino M. Combined collapse by bridging and self-adhesion in a prototypical polymer model inspired by the bacterial nucleoid. *Soft Matter.* 2015;11(9):1677–87. <https://doi.org/10.1039/c4sm02434f> PMID: 25532064
43. Shendruk TN, Bertrand M, de Haan HW, Harden JL, Slater GW. Simulating the entropic collapse of coarse-grained chromosomes. *Biophys J.* 2015;108(4):810–20. <https://doi.org/10.1016/j.bpj.2014.11.3487> PMID: 25692586
44. Chaboche Q, Campos-Villalobos G, Giunta G, Dijkstra M, Cosentino Lagomarsino M, Scolari VF. A mean-field theory for predicting single polymer collapse induced by neutral crowders. *Soft Matter.* 2024;20(15):3271–82. <https://doi.org/10.1039/d3sm01522j> PMID: 38456237
45. Seibel GL, Singh UC, Kollman PA. A molecular dynamics simulation of double-helical B-DNA including counterions and water. *Proc Natl Acad Sci U S A.* 1985;82(19):6537–40. <https://doi.org/10.1073/pnas.82.19.6537> PMID: 3863112
46. Langley DR, Doyle TW, Beveridge DL. The dymycin-DNA intercalation complex: a model based on DNA affinity cleavage and molecular dynamics simulation. *J Am Chem Soc.* 1991;113(12):4395–403. <https://doi.org/10.1021/ja00012a004>
47. Cheatham TEI, Miller JL, Fox T, Darden TA, Kollman PA. Molecular dynamics simulations on solvated biomolecular systems: the particle mesh ewald method leads to stable trajectories of DNA, RNA, and proteins. *J Am Chem Soc.* 1995;117(14):4193–4. <https://doi.org/10.1021/ja00119a045>
48. Rakers C, Bermudez M, Keller BG, Mortier J, Wolber G. Computational close up on protein–protein interactions: how to unravel the invisible using molecular dynamics simulations?. *WIREs Comput Mol Sci.* 2015;5(5):345–59. <https://doi.org/10.1002/wcms.1222>
49. Korolev N, Nordenskiöld L. H4 histone tail mediated DNA–DNA interaction and effects on DNA structure, flexibility, and counterion binding. A molecular dynamics study. *Biopolymers.* 2007;86(5–6):409–23.
50. Ponomarev SY, Thayer KM, Beveridge DL. Ion motions in molecular dynamics simulations on DNA. *Proc Natl Acad Sci U S A.* 2004;101(41):14771–5. <https://doi.org/10.1073/pnas.0406435101> PMID: 15465909
51. Spiriti J, van der Vaart A. DNA binding and bending by Sac7d is stepwise. *Chembiochem.* 2013;14(12):1434–7. <https://doi.org/10.1002/cbic.201300264> PMID: 23853062
52. van der Vaart A. Coupled binding–bending–folding: The complex conformational dynamics of protein–DNA binding studied by atomistic molecular dynamics simulations. *Biochim Biophys Acta.* 2015;1850(5):1091–8. <https://doi.org/10.1016/j.bbagen.2014.08.009> PMID: 25161164
53. Jumper J, Evans R, Pritzel A, Green T, Figurnov M, Tunyasuvunakool K, et al. AlphaFold 2. In: Fourteenth Critical Assessment of Techniques for Protein Structure Prediction. 2020. 13.
54. Jumper J, Evans R, Pritzel A, Green T, Figurnov M, Ronneberger O, et al. Highly accurate protein structure prediction with AlphaFold. *Nature.* 2021;596(7873):583–9. <https://doi.org/10.1038/s41586-021-03819-2> PMID: 34265844
55. Kim AR, Hu Y, Comjean A, Rodiger J, Mohr SE, Perrimon N. Enhanced protein–protein interaction discovery via AlphaFold–Multimer. *BioRxiv.* 2024. 2024-02.
56. Abriata LA. The Nobel Prize in Chemistry: past, present, and future of AI in biology. *Commun Biol.* 2024;7(1):1409. <https://doi.org/10.1038/s42003-024-07113-5> PMID: 39472680
57. Abramson J, Adler J, Dunger J, Evans R, Green T, Pritzel A, et al. Accurate structure prediction of biomolecular interactions with AlphaFold 3. *Nature.* 2024;630(8016):493–500. <https://doi.org/10.1038/s41586-024-07487-w> PMID: 38718835
58. Zerze GH, Stillinger FH, Debenedetti PG. Thermodynamics of DNA hybridization from atomistic simulations. *J Phys Chem B.* 2021;125(3):771–9. <https://doi.org/10.1021/acs.jpcc.0c09237> PMID: 33434025
59. Sun T, Mirzoev A, Minhas V, Korolev N, Lyubartsev AP, Nordenskiöld L. A multiscale analysis of DNA phase separation: from atomistic to mesoscale level. *Nucleic Acids Res.* 2019;47(11):5550–62. <https://doi.org/10.1093/nar/gkz377> PMID: 31106383
60. Sun T, Minhas V, Korolev N, Mirzoev A, Lyubartsev AP, Nordenskiöld L. Bottom-up coarse-grained modeling of DNA. *Front Mol Biosci.* 2021;8:645527. <https://doi.org/10.3389/fmolb.2021.645527> PMID: 33816559
61. Skoruppa E, Schiessel H. Systematic coarse-graining of sequence-dependent structure and elasticity of double-stranded DNA. *Phys Rev Research.* 2025;7(1). <https://doi.org/10.1103/physrevresearch.7.013044>
62. Odijk T. Dynamics of the expanding DNA nucleoid released from a bacterial cell. *Physica A: Statistical Mechanics and its Applications.* 2000;277(1–2):62–70. [https://doi.org/10.1016/s0378-4371\(99\)00556-7](https://doi.org/10.1016/s0378-4371(99)00556-7)
63. Rautu SA, Zidovska A, Shelley MJ. Spatiotemporal dynamics of nucleocytoplasmic transport. *Phys Rev Research.* 2024;6(4). <https://doi.org/10.1103/physrevresearch.6.043022>

64. Rautu SA, Zidovska A, Saintillan D, Shelley MJ. Active hydrodynamic theory of euchromatin and heterochromatin. 2025. <https://arxiv.org/abs/250320964>
65. Schmid F. Understanding and modeling polymers: the challenge of multiple scales. *ACS Polym Au*. 2022;3(1):28–58. <https://doi.org/10.1021/acspolymersau.2c00049>
66. Chirico G, Langowski J. Kinetics of DNA supercoiling studied by Brownian dynamics simulation. *Biopolymers*. 1994;34(3):415–33. <https://doi.org/10.1002/bip.360340313>
67. Sottas PE, Larquet E, Stasiak A, Dubochet J. Brownian dynamics simulation of DNA condensation. *Biophys J*. 1999;77(4):1858–70. [https://doi.org/10.1016/S0006-3495\(99\)77029-3](https://doi.org/10.1016/S0006-3495(99)77029-3) PMID: 10512808
68. Lu W, Onuchic JN, Di Pierro M. An associative memory Hamiltonian model for DNA and nucleosomes. *PLoS Comput Biol*. 2023;19(3):e1011013. <https://doi.org/10.1371/journal.pcbi.1011013> PMID: 36972316
69. Vologodskii A. Brownian dynamics simulation of knot diffusion along a stretched DNA molecule. *Biophys J*. 2006;90(5):1594–7. <https://doi.org/10.1529/biophysj.105.074682> PMID: 16361333
70. Gilbert BR, Thornburg ZR, Brier TA, Stevens JA, Grunewald F, Stone JE, et al. Dynamics of chromosome organization in a minimal bacterial cell. *Front Cell Dev Biol*. 2023;11:1214962. <https://doi.org/10.3389/fcell.2023.1214962> PMID: 37621774
71. Rosa A, Everaers R. Structure and dynamics of interphase chromosomes. *PLoS Comput Biol*. 2008;4(8):e1000153. <https://doi.org/10.1371/journal.pcbi.1000153> PMID: 18725929
72. Papale A, Holcman D. Chromatin phase separated nanoregions explored by polymer cross-linker models and reconstructed from single particle trajectories. *PLoS Comput Biol*. 2024;20(1):e1011794. <https://doi.org/10.1371/journal.pcbi.1011794> PMID: 38266036
73. Joyeux M. Coarse-grained model of the demixing of DNA and non-binding globular macromolecules. *J Phys Chem B*. 2017;121(26):6351–8. <https://doi.org/10.1021/acs.jpcc.7b03011> PMID: 28599107
74. Joyeux M. Bacterial nucleoid: interplay of DNA demixing and supercoiling. *Biophysical Journal*. 2020;118(9):2141–50.
75. Banani SF, Lee HO, Hyman AA, Rosen MK. Biomolecular condensates: organizers of cellular biochemistry. *Nat Rev Mol Cell Biol*. 2017;18(5):285–98. <https://doi.org/10.1038/nrm.2017.7> PMID: 28225081
76. Alberti S, Gladfelter A, Mittag T. Considerations and challenges in studying liquid-liquid phase separation and biomolecular condensates. *Cell*. 2019;176(3):419–34. <https://doi.org/10.1016/j.cell.2018.12.035> PMID: 30682370
77. Goodsell DS, Autin L. Integrative modeling of JCVI-Syn3A nucleoids with a modular approach. *Curr Res Struct Biol*. 2023;7:100121. <https://doi.org/10.1016/j.crstbi.2023.100121> PMID: 38221989
78. Hutchison CA 3rd, Chuang R-Y, Noskov VN, Assad-Garcia N, Deerinck TJ, Ellisman MH, et al. Design and synthesis of a minimal bacterial genome. *Science*. 2016;351(6280):aad6253. <https://doi.org/10.1126/science.aad6253> PMID: 27013737
79. Breuer M, Earnest EE, Merryman C, Wise KS, Sun L, Lynott MR, et al. Essential metabolism for a minimal cell. *Elife*. 2019;8:e36842. <https://doi.org/10.7554/eLife.36842> PMID: 30657448
80. Sivasankar VS, Zia RN. The matter/life nexus in biological cells. *Annu Rev Chem Biomol Eng*. 2025;16(1):409–32. <https://doi.org/10.1146/annurev-chembioeng-100722-104442> PMID: 40489303
81. Nadeau JG, Crothers DM. Structural basis for DNA bending. *Proc Natl Acad Sci U S A*. 1989;86(8):2622–6. <https://doi.org/10.1073/pnas.86.8.2622> PMID: 2704739
82. Vologodskii A. *Biophysics of DNA*. Cambridge University Press; 2015.
83. Joyeux M. Preferential localization of the bacterial nucleoid. *Microorganisms*. 2019;7(7):204. <https://doi.org/10.3390/microorganisms7070204> PMID: 31331025
84. Dame RT, Goosen N. HU: promoting or counteracting DNA compaction?. *FEBS Lett*. 2002;529(2–3):151–6. [https://doi.org/10.1016/s0014-5793\(02\)03363-x](https://doi.org/10.1016/s0014-5793(02)03363-x) PMID: 12372591
85. Ryu BK, Zia RN. Size-selective characterization of porous media via tortuous network analysis. *Journal of Rheology*. 2022;66(1):219–33. <https://doi.org/10.1122/8.0000359>
86. Xiang Y, Surovtsev IV, Chang Y, Govers SK, Parry BR, Liu J, et al. Interconnecting solvent quality, transcription, and chromosome folding in *Escherichia coli*. *Cell*. 2021;184(14):3626–3642.e14. <https://doi.org/10.1016/j.cell.2021.05.037> PMID: 34186018
87. Milchev A, Egorov SA, Nikoubashman A, Binder K. Conformations and orientational ordering of semiflexible polymers in spherical confinement. *J Chem Phys*. 2017;146(19):194907. <https://doi.org/10.1063/1.4983131> PMID: 28527445
88. Elam WT, Kerstein AR, Rehr JJ. Critical properties of the void percolation problem for spheres. *Phys Rev Lett*. 1984;52(17):1516–9. <https://doi.org/10.1103/physrevlett.52.1516>
89. Wang G, Zhu C, Fu T, Ma Y. Formation mechanism and criterion of tail satellite droplets for moving droplet in microchannel. *Chemical Engineering Science*. 2021;238:116607. <https://doi.org/10.1016/j.ces.2021.116607>
90. Frenkel D. Order through disorder: entropy strikes back. *Phys World*. 1993;6(2):24–5. <https://doi.org/10.1088/2058-7058/6/2/24>
91. Gibbs JW. *Elementary principles in statistical mechanics: developed with especial reference to the rational foundations of thermodynamics*. C. Scribner's Sons; 1902.
92. Dougherty J. Lectures on gas theory. *Journal of Fluid Mechanics*. 1964;20(4):698–9.

93. Kominami H, Kobayashi K, Yamada H. Molecular-scale visualization and surface charge density measurement of Z-DNA in aqueous solution. *Sci Rep*. 2019;9(1):6851. <https://doi.org/10.1038/s41598-019-42394-5> PMID: 31048715
94. Dutagaci B, Nawrocki G, Goodluck J, Ashkarran AA, Hoogstraten CG, Lapidus LJ, et al. Charge-driven condensation of RNA and proteins suggests broad role of phase separation in cytoplasmic environments. *Elife*. 2021;10:e64004. <https://doi.org/10.7554/eLife.64004> PMID: 33496264
95. Schavemaker PE, Śmigiel WM, Poolman B. Ribosome surface properties may impose limits on the nature of the cytoplasmic proteome. *Elife*. 2017;6:e30084. <https://doi.org/10.7554/eLife.30084> PMID: 29154755
96. Ishihama Y, Schmidt T, Rappsilber J, Mann M, Hartl FU, Kerner MJ, et al. Protein abundance profiling of the Escherichia coli cytosol. *BMC Genomics*. 2008;9:102. <https://doi.org/10.1186/1471-2164-9-102> PMID: 18304323
97. Roure G, Zinchenko AZ, Davis RH. Numerical simulation of deformable droplets in three-dimensional, complex-shaped microchannels. *Physics of Fluids*. 2023;35(10). <https://doi.org/10.1063/5.0162881>
98. Roure G, Davis RH. Permeation network model for the swelling of Water-in-Oil-in-Water (W/O/W) emulsions. *Ind Eng Chem Res*. 2024;64(1):788–96. <https://doi.org/10.1021/acs.iecr.4c02588>
99. Hofmann JL, Yang TS, Sunol AM, Zia RN. Protein-protein interactions facilitate transport of translation molecules in Escherichia coli: the roles of valency, affinity, and crowding. *Biophysical Journal*. 2023;122(3):489a. <https://doi.org/10.1016/j.bpj.2022.11.2617>
100. Wang JG, Dhumal U, Zakhari MEA, Zia RN. Probing the elusive equilibrium crystal/liquid coexistence state in monodisperse hard-sphere colloids simulations. 2025.
101. Zia RN, Landrum BJ, Russel WB. A micro-mechanical study of coarsening and rheology of colloidal gels: cage building, cage hopping, and Smoluchowski's ratchet. *Journal of Rheology*. 2014;58(5):1121–57. <https://doi.org/10.1122/1.4892115>
102. Cunha LHP, Zhao J, MacKintosh FC, Biswal SL. Settling dynamics of Brownian chains in viscous fluids. *Phys Rev Fluids*. 2022;7(3):034303. <https://doi.org/10.1103/physrevfluids.7.034303>
103. Wennerström H, Vallina Estrada E, Danielsson J, Oliveberg M. Colloidal stability of the living cell. *Proc Natl Acad Sci U S A*. 2020;117(19):10113–21. <https://doi.org/10.1073/pnas.1914599117> PMID: 32284426
104. Roure G. Microhydrodynamics of droplets and particles: applications in microfluidics and agglomeration. University of Colorado at Boulder; 2023.
105. Sunol AM, Zia RN. Confined Brownian suspensions: equilibrium diffusion, thermodynamics, and rheology. *Journal of Rheology*. 2023;67(2):433–60. <https://doi.org/10.1122/8.0000520>
106. Patrone PN, Rosch TW. Beyond histograms: efficiently estimating radial distribution functions via spectral Monte Carlo. *J Chem Phys*. 2017;146(9):094107. <https://doi.org/10.1063/1.4977516> PMID: 34234386
107. Thompson AP, Aktulga HM, Berger R, Bolintineanu DS, Brown WM, Crozier PS, et al. LAMMPS - a flexible simulation tool for particle-based materials modeling at the atomic, meso, and continuum scales. *Computer Physics Communications*. 2022;271:108171. <https://doi.org/10.1016/j.cpc.2021.108171>